Title

Mechanosensitive Adhesion Explains Stepping Motility in Amoeboid Cells

Permalink

https://escholarship.org/uc/item/31k9s95q

Journal

Biophysical Journal, 112(12)

ISSN

0006-3495

Authors

Copos, Calina A
Walcott, Sam
del Álamo, Juan C
et al.

Publication Date

2017-06-01

DOI

10.1016/j.bpj.2017.04.033

Peer reviewed

Mechanosensitive adhesion explains stepping motility in amoeboid cells

C. A. Copos, S. Walcott, J. C. del Álamo, E. Bastounis, A. Mogilner, R. D. Guy

Abstract

Cells employing amoeboid motility exhibit repetitive cycles of rapid expansion and contraction and apply coordinated traction forces to their environment. Though aspects of this process are well studied, it is unclear how the cell controls the coordination of cell length changes with adhesion to the surface. Here, we develop a simple model to mechanistically explain the emergence of periodic changes in length and spatiotemporal dynamics of traction forces measured in chemotaxing uni-cellular amoeba, *Dictyostelium discoideum*. In contrast to the biochemical mechanisms that have been implicated in the coordination of some cellular processes, we show that many features of amoeboid locomotion emerge from a simple mechanochemical model. The mechanism for interaction with the environment in *Dictyostelium* is unknown and thus, we explore different cell-environment interaction models to reveal that mechanosensitive adhesions are necessary to reproduce the spatiotemporal adhesion patterns. In this modeling framework, we find that the other motility modes, such as smooth gliding, arise naturally with variations in the physical properties of the surface. Thus, our work highlights the prominent role of biomechanics in determining the emergent features of amoeboid locomotion.

Key words: cell migration, amoeboid locomotion, mechanosensing, biomechanics, computational models, chemotaxis.

Introduction

Cell movement is required in many physiological and pathological processes such as the immune system response and cancer metastasis [1, 2]. One of a broad spectrum of migratory mechanisms is amoeboid migration, characterized by repetitive cycles of fast shape changes. The prototypical example is a chemotaxing single-cell amoeba *Dictyostelium discoideum* [3], but similar mechanisms are employed by neutrophils, lymphocytes, and some tumor cells [4–7]. These rapid shape changes occur periodically and in coordination with traction forces that drive cell locomotion, allowing these cells to quickly adapt to different environments and develop rapid velocities [8–10]. Although key molecular processes involved in amoeboid locomotion are known, it remains unclear how these processes are coordinated to give rise to this form of migration [3, 11].

Amoeboid movement is exhibited by the amoeba, *Dictyostelium*, chemotaxing on flat surfaces. Here, we present typical measurements of the traction stresses and cell length of the crawling amoeba as those measured in [10, 12]. In the presence of a chemoattractant gradient, a motility cycle is initiated through polymerization of actin filaments at the leading edge [13, 14]. The four phases of this motility cycle are [3, 6]: (1) a pseudopod forms as the cell body elongates (increase in cell length), (2) the pseudopod adheres to the substrate through mechanisms that remain to be identified (cell length reaches a maximum), (3) the cell body contracts after pseudopod attachment (decrease in cell length), and (4) the cell rear retracts and detaches as the adhesive links at the rear of the cell release and allow advancement of the cell body (cell length reaches a minimum). Notably, the phases of the motility cycle correlate with the cyclic lengthening-shortening events observed in measurements of *Dictyostelium* body length over time (Fig. 1A) [10].

The traction forces applied on the surface by the crawling cell are also correlated with the phases of the motility cycle (Fig. 1B) [12]. Regions of elevated traction forces are thought to be indicators of where the cell adheres to the substrate [15, 16], so that *Dictyostelium* adheres to the substrate in either 2 or 3 distinct physical locations (Fig. 1B). Generally, axial stresses are negative at the cell front (directed inward toward the cell rear) and positive at the cell rear (directed inward toward the front). Shortly after a new pseudopod forms, the cell establishes a new adhesion site under the nascent pseudopod. The 'old' front adhesion site becomes the 'new' back adhesion site, while the 'old' back adhesion site is lost once the cell passes its position. Thus, the front adhesion site is 'recycled' to a back adhesion site, as indicated by the horizontal bands of elevated forces with a lifetime similar to the period of the motility cycle (Fig. 1B). While the evidence is clear that adhesion sites do not form randomly but have well-defined dynamics that are synchronized with the phases of the motility cycle [8, 9, 12] (Fig. 1C), the mechanism responsible for these spatiotemporal adhesion patterns is unknown. Further, the molecules involved in generating adhesive forces are also unknown [17, 18].

The synchronization of adhesion dynamics with periodic length changes causes *Dictyostelium* to engage in step-like locomotion; as the cell crawls, it forms sequential adhesion sites that remain fixed on the surface and stable during the motility cycle. Interestingly, this stepping motion is robust as illustrated by the analysis of five mutant strains of *Dictyostelium* which shows that these cells also exhibit step-like movement and, furthermore, regulate their locomotion so that the 'stride length' is insensitive to cell type (Fig. 1D) [10, 19]. Together, these observations imply that the migration speed is determined by a highly coordinated yet well-conserved mechanism involving actin polymerization for pseudopod extension, contraction of the cell body, together with a synchronized mechanism for attachment and detachment of adhesions to the surrounding environment. In particular, we are motivated by questions of how these key cellular process achieve front-to-back coordination and the emergent periodic cycles of cell length changes that are needed for locomotion. We are also interested in understanding how these intracellular processes are synchronized with the formation and rupture of adhesions to the surface to give rise to the reported spatiotemporal dynamics of traction forces.

While biochemical mechanisms have long been thought to underlie aspects of cell motility, recent work has also implicated biomechanical mechanisms [20–23]. Here, we hypothesize that the periodic morphological changes emerge from the force-dependent action of actin polymerization at the leading edge, the mechanical response of the outer cell membrane and its underlying actomyosin cortex, together with a force-sensitive interaction with the surface. In support of this hypothesis, we present a simple mechanochemical model which

captures all observed features of amoeboid locomotion: spatiotemporal distribution of traction stresses, recycling of cell-substrate adhesions, and the emergence of periodic lengthening-shortening events. An exploration of different cell-environment interaction models reveals that mechanosensitive adhesions are necessary to explain the localization and recycling of adhesion sites during a motility cycle. Further, when adhesion and surface parameters are varied other experimentally observed motility modes emerge in our model.
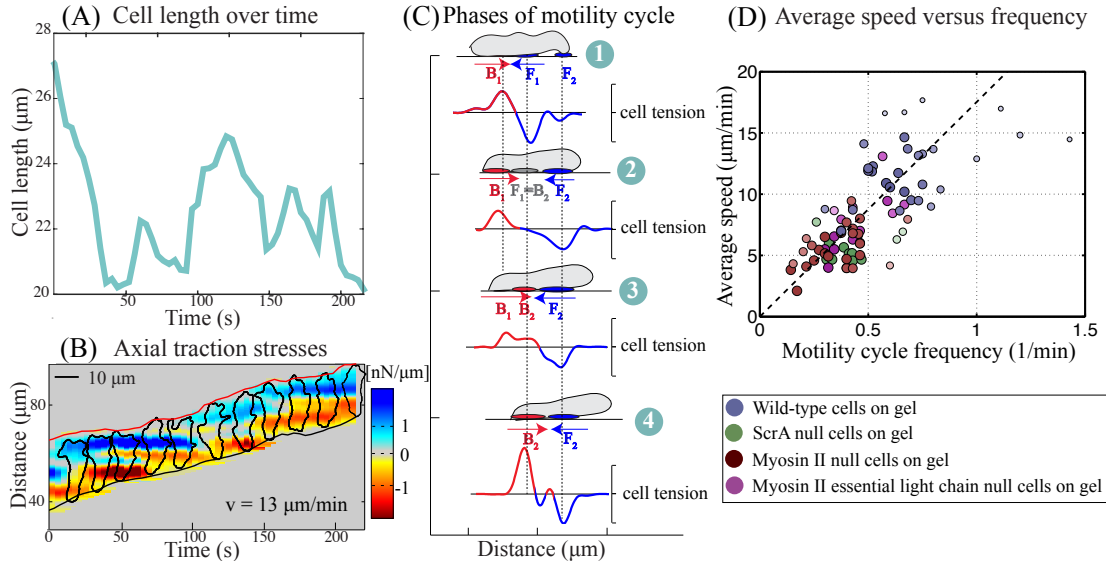

Figure 1: **Features of amoeboid motility exemplified by the chemotaxing uni-cellular *Dictyostelium* amoeba.** (A) The plot of the body length over time shows periodic lengthening-shortening events. (B) Spatiotemporal representation of the instantaneous magnitude of the tangential tensions (force per length) as a function of the position along the cell trajectory (vertical axis) and time (horizontal axis) for a representative wild-type *Dictyostelium* cell. The tension measurements yield from integrating axial stresses across the cell width and we use these tensions to understand the traction stresses involved in motion. (C) Schematic representation showing the four phases of motility cycle with snapshots of the instantaneous cell shape, location and magnitude of traction adhesions and axial tensions. Front and back adhesions are shown as blue and red ovals underneath the cell while the gray oval represents weak adhesions. The numbers correspond to the phases of the motility cycle. (D) Scatter plot of the average migration speed as a function of the frequency of the motility cycle for different mutants. The dashed line is the least squares fit to the data, $v = 18f$ showing that the cells perform a motility cycle with an average step length of 18 μm. The circles represent individual cells but to better visualize the correlation, the f-v plane was divided into rectangular tiles of equal area, and the size and color of each data point were scaled according to the total number of data points that fall on each specific tile (i.e., its rate of occurrence). As a result, darker, larger circles represent those data points that were observed more often in our experiments, and vice versa. Statistical information for the stride length per cell type is presented in supplementary material Fig. S5. Details for experimental data acquisition are in supplementary material S.1.

Methods

Model

We developed a continuous two-dimensional mechanical model of an amoeboid cell polarized in a fixed direction (Fig. 2). The cell crawls in the horizontal direction with surface attachments between the cell and the surface below it. The outer cell membrane and its underlying actomyosin cortex are represented as a single
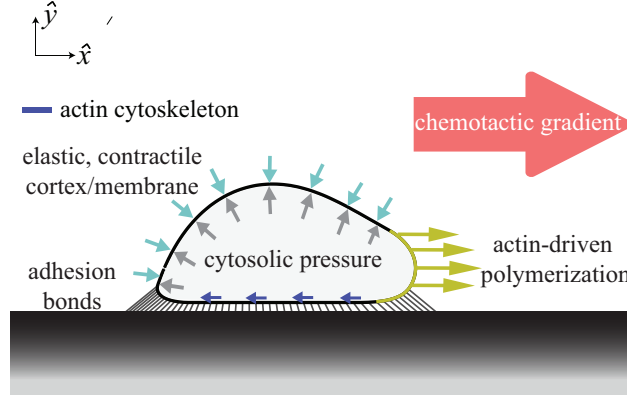
Figure 2: **A schematic of model.** Side view of a *Dictyostelium* cell polarized in a fixed direction of a chemotactic gradient. Our mechanical model of an amoeboid cell has four cellular components: (1) combined membrane-cortex structure, (2) viscous cytosol, (3) actin-driven polymerization at the leading edge, and (4) interaction with the substrate. The arrows along the ventral surface of the cell represent the action of the actin cytoskeleton.

structure with position $\boldsymbol{X}(s,t) = (x(s,t), y(s,t))$ where t is time and s is the local parametric coordinate on the structure. Here, $\hat{x}$ is a unit vector in the horizontal direction of crawling while $\hat{y}$ is in the vertical direction. The cell cytoplasm is represented as a viscous fluid with instantaneously equilibrated internal pressure. Our model consists of a balance of forces involving the response of the combined membrane-cortex structure, the interaction force between the cell and the surface, the intracellular pressure that enforces volume incompressibility of the cell, the polymerization machinery driving the forward motion, the cytoskeleton that transmits polymerization forces to the underlying surface, and a viscous drag force with the surrounding environment:

$$\xi \frac{\partial \boldsymbol{X}}{\partial t} = \boldsymbol{F}_{\text{membrane/cortex}} + \boldsymbol{F}_{\text{pressure}} + \boldsymbol{F}_{\text{polymerization}} + \boldsymbol{F}_{\text{cytoskeleton}} + \boldsymbol{F}_{\text{surface}} . \tag{1}$$

Here, we assume a velocity-dependent drag with the environment where ξ denotes the viscous drag coefficient. We now focus on the constitutive laws of these cellular forces.

Outer cell membrane and actomyosin cortex

The cell membrane and the actomyosin cortex structure are treated as a single elastic, contractile structure [24, 25]. The elastic force density is computed by $\boldsymbol{F}_{\text{membrane/cortex}} = \frac{\partial}{\partial s}(T\hat{\tau})$ where T is tension and $\hat{\tau}$ is the tangent vector to the curve $\boldsymbol{X}(s,t)$. The tension is given by $T = \gamma + k(|\partial \boldsymbol{X}/\partial s| - 1)$ which describes a linearly elastic spring with stiffness k and resting tension γ.

Intracellular fluid

The cytosol is modeled as a viscous medium and is assumed to have a resting internal pressure p_0 and resting volume V_0. The pressure force is given by, $\boldsymbol{F}_{\text{pressure}} = (p_0 + \kappa_{\text{cell}} \ln(V/V_0)) \hat{n}$ where $\hat{n}$ denotes the outward normal unit vector and κ_{cell} is a bulk modulus. Given the other forces acting on the membrane-cortex, the resting pressure is selected to ensure cell volume conservation, $\int \boldsymbol{F} \cdot \hat{n} \, ds = \xi \int \partial \boldsymbol{X}/\partial t \cdot \hat{n} \, ds = 0$, while the volumetric correction term further ensures volume conservation is maintained throughout the simulation.

Actin-driven polymerization

The mechanical origin of these protrusive forces caused by directional polymerization of F-actin filaments is a well-studied problem [21]. It has been shown that branching actin networks have a force-velocity relation at the leading edge, $v = v(F_L)$, where F_L is the force against the protrusion [26–28]. In the region of polymerization,

we assume the following one-dimensional model for the leading edge velocity due to directional polymerization of F-actin filaments against the cell membrane,

$$v = \rho_1 e^{-\rho_2 F_L} - \rho_3 \ . \tag{2}$$

Force-velocity relations of this form were observed theoretically [21] and experimentally in a certain region of the load forces [26–28]. Here, $\rho_{1,2,3}$ are parameters from measurements of the force-velocity relation at the leading edge. An equivalent way to formulate this relation is to assume the polymerization force is a function of the protrusion rate: $F_{\text{polymerization}} = F_{\text{polymerization}}(v)$. Then, the force-balance equation in the direction of motion (Eq. 1) at the cell front has the form:

$$F_{\text{polymerization}}(v) + F_L = \xi v \ . \tag{3}$$

Together, Eqs. 2-3, describe our one-dimensional model for driving the cell front forward. We compute F_L as the average magnitude of the forces on the membrane-cortex structure in the region of polymerization, and solving Eq. 3 determines the leading edge velocity at each time step. Details of implementation in the two-dimensional case are discussed in Supplemental Material, S.2.

Unlike cell types which form thin, actin-rich lamellipodia to crawl, in *Dictyostelium*, actin polymerization occurs in a large frontal region corresponding to roughly 20-30% of the cell length [29]. Accordingly, we define the region of polymerization, $\mathcal{P}$, as a region of fixed arclength of 21% of the undeformed membrane-cortex boundary centered about the horizontal extremum of the boundary (yellow line in Fig. 2).

Cytoskeleton

The cytoskeleton transmits the polymerization forces to the surface; the protrusive forces at the leading edge are integrated over the region of polymerization and distributed uniformly to the region of cell-surface contact to ensure zero sum of polymerization and cytoskeletal forces,

$$\boldsymbol{F}_{\text{cytoskeleton}} = -\frac{\int_{\mathcal{P}} |\boldsymbol{F}_{\text{polymerization}}|\, ds}{\int_{\mathcal{C}} ds}\, \widehat{x} \ .$$

The membrane-cortex structure is defined to be in the region of contact, $\mathcal{C}$, if it is within 5 μm of the substrate in the vertical direction. Without this model of the cytoskeleton, the driving forces would be unbalanced.

Cell-surface interaction

We assume the cell crawls on top of a flat rigid surface along the horizontal axis. The cell interacts with an underlying flat surface through both physical adhesive connections and a repulsive force due to contact with the surface: $\boldsymbol{F}_{\text{surface}} = \boldsymbol{F}_{\text{steric}} + \boldsymbol{F}_{\text{adhesion}}$. Below a certain distance, δ_w, the cell feels a nonspecific steric force of the form: $\boldsymbol{F}_{\text{steric}} = -k_{\text{steric}} \left(|y(s,t)| - \delta_w \right) \widehat{y}$ with k_{steric} represents a stiffness of the steric interaction.

Little is known about the adhesion kinetics in *Dictyostelium*, and thus the form of the adhesion force is the main object of our investigation. In this paper, we explore models for the adhesive force resulting from the distribution of bonds that behave as elastic linear springs: $\boldsymbol{F}_{\text{adhesion}} = \zeta N(t,s)(|\boldsymbol{X} - \boldsymbol{X}_{\text{surface}}|/\ell_0 - 1)\, (\boldsymbol{X} - \boldsymbol{X}_{\text{surface}})/|\boldsymbol{X} - \boldsymbol{X}_{\text{surface}}|$, where ℓ_0 is the length of the spring in its undeformed state and $\boldsymbol{X}_{\text{surface}}$ are locations along the flat substrate. The position of $\boldsymbol{X}_{\text{surface}}$ is determined per bond during bond formation; when an adhesive bond forms it binds to the surface directly below the membrane-cortex structure. For the lifetime of the bond, the binding position remains fixed along the surface. At each site, the adhesive force is the result of the local bond density per adhesion site, $N(t,s)$, and a constant adhesive stiffness, ζ. In the paper, we will consider models with dynamic bond formation and rupture; thus, the local bond density can vary between zero to full occupancy of a site, $0 \le N(t,s) \le 1$.

The full model and the discretization method are in supplementary material S.2. Model parameters are provided in supplementary material, Table S1.

Motility assumptions

Our modeling hypothesis is that mechanics drive both the cycles of extension-contraction of the cytoskeleton and coordinated adhesion kinetics in order to give rise to the complex and highly-synchronized features of stepping amoeboid motility. To reveal the mechanism responsible for these two processes and their coordination through biomechanics, we make minimal modeling assumptions and introduce complexity in the constitutive laws of mechanical forces as motivated by the results of the simulations.

During pseudopod extension, experimental data of traction forces *Dictyostelium* show that the pseudopod does not initially attach to the surface [12, 30]. Motivated by these observations, the simulated pseudopod must achieve a minimal length of 10 μm before attachment. Once the length condition is met, proximity to surface determines if discrete points are available for binding. While symmetry of the problem is broken by polymerization at the leading edge, in order to move the cell needs to communicate leading edge forces to the cell rear and rupture back adhesions. The rupture of adhesions is assumed to be force-sensitive and modeled as a piecewise constant function,

$$\boldsymbol{F}_{\text{adhesion}} = \begin{cases} \zeta N(t,s)(|\boldsymbol{X} - \boldsymbol{X}_{\text{surface}}|/\ell_0 - 1)\frac{\boldsymbol{X} - \boldsymbol{X}_{\text{surface}}}{|\boldsymbol{X} - \boldsymbol{X}_{\text{surface}}|} & \text{if } \frac{|\boldsymbol{F}_{\text{adhesion}}|}{N} < F_{\text{critical}} \\ 0 & \text{otherwise,} \end{cases} \tag{4}$$

for a threshold adhesive load, F_{critical}. Adhesions can break at any spatial or temporal location and no biochemical coordination between the front and the rear of the cell is prescribed. The formation of adhesions is determined by the proximity of the membrane-cortex structure to the surface. In the following sections, we explore three models for cell-substrate adhesion interaction: (1) spatially uniform adhesions with fixed bond density, (2) spatially non-uniform adhesions with fixed bond density, and lastly (3) uniform adhesions with dynamic bond density. Details of adhesion models and the resulting motion are discussed later.

Results

Traction patterns for a simulated cell with uniformly distributed adhesions

Initially, adhesions are modeled by linearly elastic springs with constant bond density of full occupancy, $N = 1$ in Eq. 4. A similar adhesion model for cell-surface interaction has been previously used to explain the dynamics of adherent cells [23, 31, 32]. We find that the mechanical model detailed above is sufficient to result in coordinated locomotion at a constant speed as indicated by the time evolution of the cell centroid (dashed line in Fig. 3A, supplementary material, Movie S1).

The resulting movement indicates that the model does capture the emergence of coordination between extension of the front and rupture of back adhesions and notably, in the absence of biochemical signaling. Here, the coordination is achieved through the mechanical response of the membrane-cortex structure. As the cell lengthens due to pseudopod extension, the elastic forces in the membrane-cortex structure become elevated. Together with the cell curvature, these elevated forces induce a strain on rear adhesions which eventually break due to their force-dependent response. While elastic forces point inward at the cell front and rear, at the front polymerization forces push outward providing partial counterbalance and thus, a bias to preferentially rupture rear adhesions. However, the emergent movement has none of the features of stepping locomotion observed in wild-type crawling cells (see Fig. 1A,B). The cell length remains relatively constant ($\sim$10% change compared to the fluctuations in Fig. 1A) and the lack of horizontal patches in the kymograph of axial stresses is evidence that adhesion sites are not fixed on the surface or recycled as the cell crawls (comparing Fig. 3A to Fig. 1B).

In the spatial distribution of traction stresses, we observe localization of forces along the cell periphery which is similar to what is observed in experimental data of traction stresses during the extension phase (Fig. 3B,C). Following the time evolution of the axial stresses, we see that as the cell elongates, back adhesions rupture one-by-one (panels 2–T in Fig. 3B). Since adhesions are everywhere on the ventral part of the cell, when the rear-most adhesion ruptures, the one immediately adjacent to it will rupture as the cell lengthens.
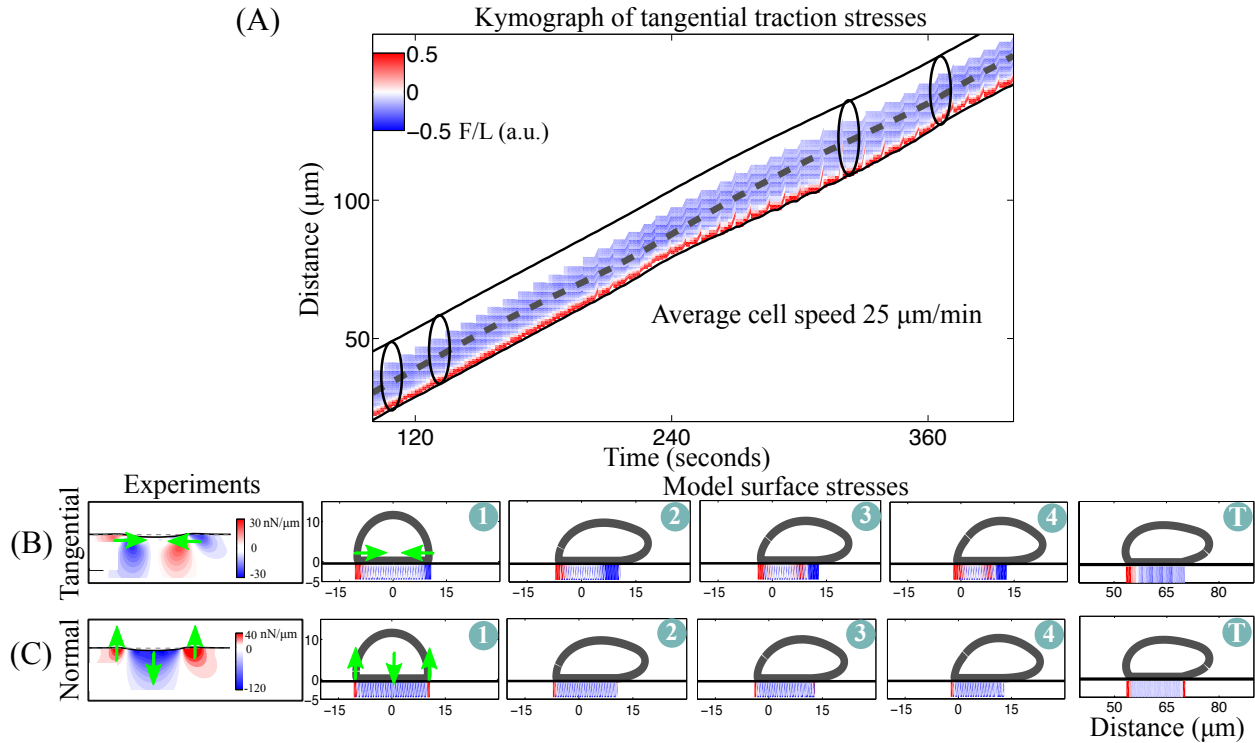
Figure 3: **A simulated cell with spatially uniform cell-surface adhesions crawls but without the features of stepping locomotion.** (A) Kymograph of axial traction stresses (force per length) as a function of the position along the cell trajectory at a given time. The constant slope of the instantaneous position of the front and back cell edges (inclined black lines) indicates small length changes. The black contours are hypothetical cell outlines at different time instances. (B, C) Snapshots of the cell outline and the corresponding tangential stresses (B) and normal stresses (C). The first panel shows experimental data during the first phase of the motility cycle. The following panels are model results at four time instances during the motility cycle and one panel later in time ($t = 179$ seconds). The green arrows indicate the direction of the forces during the first phase of the cycle.

This results in a gradual gliding of the back with adhesions that form and disappear as the cell moves across the surface. In fact, gliding locomotion is exhibited by *Dictyostelium* cells when placed on poly-L-lysine coated surfaces (supplementary material, Fig. S6). We presume this is because the increased nonspecific cell-surface interaction on this substrate results in spatially uniform interaction. More generally, stepping motility must arise from more complex dynamics than uniformly distributed, linearly elastic springs with force-dependent rupture.

A non-uniform spatial distribution of adhesions is required for stepping motility

In the previous adhesion model, the small morphological changes can be attributed to the lack of a contraction in the cell body due to a continual gliding of the cell rear. One way to prevent gliding and achieve length contraction is to assume that there are no adhesions near the center, thus prescribing a non-uniform spatial distribution of adhesions. With no consideration to how this non-uniformity is achieved, we test this hypothesis by comparing the cell length and spatiotemporal dynamics of axial stresses in the two models: uniform and non-uniform distribution of adhesions (Fig. 4). The non-uniform spatial distribution of adhesions is prescribed by fixing the bond density to be nonzero only in a region 6 μm from the cell front and rear (as illustrated in Fig. 4B.1).
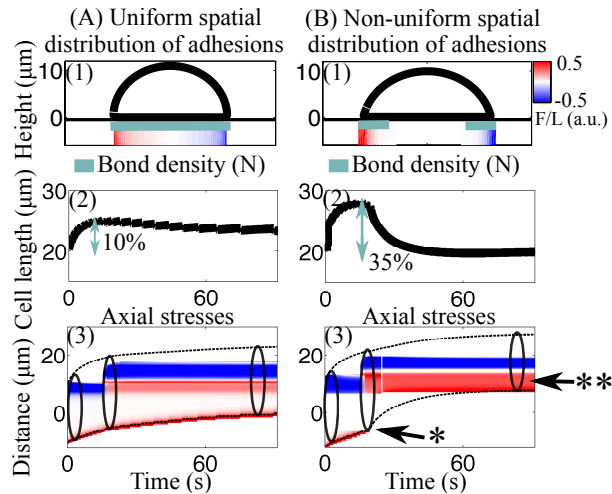
Figure 4: **Comparison of emerging motility when varying the spatial distribution of adhesions**. For these simulations the cell is polymerizing for only 60 seconds. (A.1) and (B.1) Cell outline along with spatial profile of tangential surface stresses. The spatial distribution of adhesion sites along the ventral part of the cell is shown by the blue line. For non-uniform distribution of adhesions, bond density is prescribed to be nonzero only in a region near the cell front and rear. (A.2) and (B.2) Time evolution of cell length; a lengthening-shortening event is captured with prescribed spatial localization of adhesions. (A.3) and (B.3). Kymographs of axial traction stresses as a function of the position along the cell trajectory at a given time. When non-uniform distribution of adhesions is assumed, the rear adhesion site is lost ($*$) and the front adhesion site remains fixed on the surface but is reused as a rear adhesion site at the end of the motility cycle ($**$).

With non-uniformly spaced adhesions, we obtain an extension-contraction event in the time evolution of cell length (Fig. 4B.2). When all of the rear adhesions rupture, the cell cannot adhere to the surface in any location other than the front, and thus the rear membrane rolls up. As the membrane-cortex structure rolls up and contracts, what was initially the front adhesion site is now located at the rear of the cell and the cell pulls upward and inward on these bonds (see supplementary material, Movie S4). The complete loss of rear adhesions immediately after pseudopod attachment can also be seen in the kymograph of axial stresses (single asterisk, Fig. 4B.3). While contraction of cell length was expected through localization of adhesions, nontrivially we also observe recycling of the front adhesion site to a back adhesion site at the same location on the surface (double asterisks, Fig. 4B.3).

The lengthening-shortening event, the complete loss of rear adhesions, and the recycling of adhesion sites suggest that this model is closer to reproducing the stepping locomotion observed in amoeboid cells. For the model to capture features of amoeboid migration, we had to assume adhesions exist only at the cell periphery, corresponding to regions of elevated axial stresses. The presence of adhesions only in regions of large stresses is also supported by traction force microscopy imaging data [8, 12, 33].

Periodic length changes emerge from a mechanosensitive cell-surface interaction

One way to achieve adhesion formation only in regions of elevated forces is by allowing bonds to form in response to an applied external load. In fact, some biological adhesive bonds are force-sensitive and can weaken (slip bonds) or strengthen (catch bonds) with applied force [34]. In particular, catch bonds are characterized by the physical property that at intermediate forces their lifetime increases with increasing force. Such bonds are found in $\alpha_5\beta_1$-integrins involved in adhesion of human-derived lymphoma cells [35] but also in cadherins which mediate cell-cell adhesion [36]. This description can be modeled in different ways and here we follow
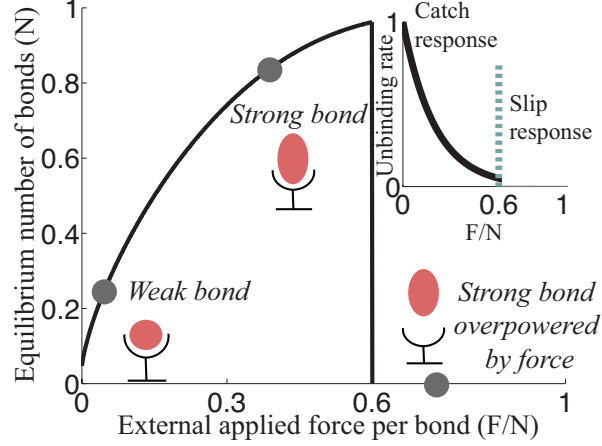
Figure 5: **Dynamics of force-sensitive bonds in a single adhesion site**. Equilibrium number of bonds per adhesion site as a function of the external applied force per bond. The inset shows the unbinding rate of a bond as a function of the applied force density. Distinct points are identified in both plots for different values of applied force density: $|\boldsymbol{F}|/N = 0.1$ (low), 0.3 (intermediate), and 0.75 (exceeds threshold load).

the form given by Novikova and Storm [37]. To incorporate force-sensitive bond kinetics, we add an equation for the time-evolution of the bond density in our existing mechanical model of a crawling cell:

$$\frac{\partial}{\partial t}N(t,s) = k^+\eta_0(1 - N) - k^- N \exp\left(-\frac{\alpha|\boldsymbol{F}|/N}{k_B T}\right). \tag{5}$$

The first term represents the formation of new bonds at a rate proportional to a constant binding rate, k^+ (M^{-1} time^{-1}) and an unsaturated substrate ligand concentration, η_0 (M). The second term represents force-dependent unbinding with a zero-force unbinding rate, k^- (time^{-1}), and a microscopic length scale characterizing the unbinding transition, α. The explicit Euler time integration scheme is used to evolve Eq. 5 at every discrete point on the ventral part of the cell, and the updated bond density is then used to compute the adhesion force in Eq. 4 locally and at every time instance.

Additionally, our model for cell-surface interaction includes the slip response of bonds through F_{critical} in Eq. 4; if the external force exceeds a threshold load, bonds immediately rupture. Under these assumptions, we find that at a low applied force, the steady-state bond density is nearly zero but as force increases, the bond density should increase as well mimicking the physical property that the bond lifetime increases with increasing force (Fig. 5). The addition of a time evolution equation for the bond density in response to an applied load reproduces the observation that *Dictyostelium* adheres to the surface in regions of large forces.

Upon including mechanosensitive bond kinetics for uniformly spaced adhesions in our model, the emerging motility is reported by the spatiotemporal patterns of the axial traction stresses and the time evolution of the cell length (Fig. 6, supplementary material, Movie S2). We chose values for adhesion parameters, k^+, k^-, F_{critical} (supplementary material, Table S1), in order to match the experimentally measured migration speed and we found that the values for these adhesion parameters are comparable to those in other cell types (supplementary material, Table S2). A parameter exploration is discussed later. We find high density bonds localized at the cell periphery, distinct and recycled adhesion sites seen by the horizontal patches in the kymograph, and periodic oscillations in cell length; these are all characteristics of stepping amoeboid motility presented in the experimental measurements in Fig. 1A,B. The simulated cell moves at a roughly constant speed of 11 μm/min (the reported values for *Dictyostelium* are 9-12 μm/min [3]). The cell undergoes repetitive lengthening-shortening cycles with a period of approximately 1 minute (the reported period for *Dictyostelium* is 0.93 minutes [12]) and

an average amplitude of 6 μm. With a periodicity similar to the period of the motility cycle ($\sim$80 seconds), a fixed location on the surface identified as a front adhesion site is recycled to a rear adhesion site (asterisk in Fig. 6). These distinct, recycled adhesion sites and periodic oscillations in cell length emerge as a result of the cell geometry, mechanical response of the cell, and force-sensitive interaction with the surface. The transmission of leading edge forces to rupture back adhesions in a coordinated manner is still established through the mechanical response of the membrane-cortex structure. The instantaneous patterns of 3D traction stresses continue to resemble the spatial arrangement of the experimental 3D traction stresses in *Dictyostelium* (inset Fig. 6A).
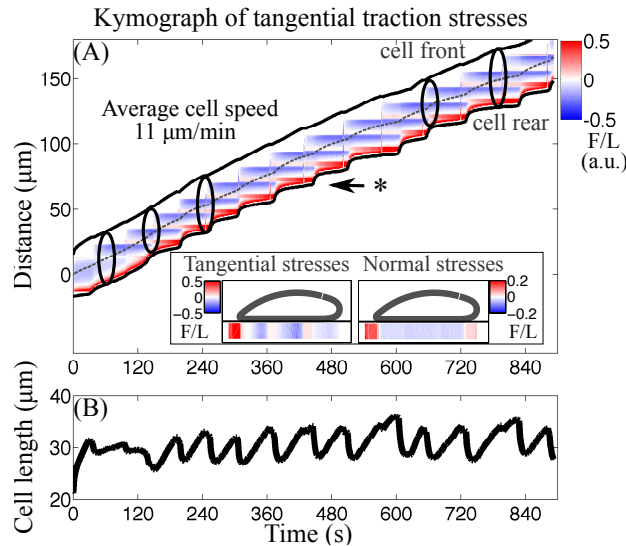

Figure 6: **Stepping locomotion observed in a simulated cell with mechanosensitive cell-surface interaction**. (A) Kymograph of the tangential traction stresses as a function of the position along the cell trajectory at a given time. The inclined lines indicate the instantaneous position of the front and rear cell edges while the dashed line represents the cell centroid position. The black outlines are hypothetical cell outlines. The asterisk shows evidence for recycling adhesions; adhesion sites are fixed on the substrate during a motility cycle. The inset shows the instantaneous spatiotemporal patterns of the tangential (left) and normal (right) traction stresses at $t = 585$ seconds. (B) The time evolution of the cell length shows periodic extension-contraction events with a period of approximately 1 minute and an average amplitude of 6 μm.

Stride length does not depend on cell mechanical parameters

We performed a series of simulations with perturbations to cellular mechanical parameters. By varying the resting tension, the elastic spring constant, and the strength of polymerization (i.e., ρ_1) individually, we obtain the averaged cell length, period of motility cycle, and migration speed (supplementary material Table S2). Based on these observations together with visual inspection of kymographs of traction stresses, we report that cells exhibit either stepping locomotion or get stuck to the surface.

The mean speed of migration is plotted as a function of the frequency of the motility cycle to reveal a linear scaling, $v = \lambda \cdot f$ (Fig. 7). The constant of proportionality, λ, represents the average step length advanced by the cell per cycle and it suggests that cells perturbed from baseline parameters not only use stepping motility but do so by preserving their stride length, $\lambda = 12 \ \mu$m. The model observation that stride length is preserved across parameter perturbations is also reported in biological mutants (Fig. 1D)) [10, 19].

Three of the perturbations to mechanical parameters show that cells get stuck to the surface. A decrease
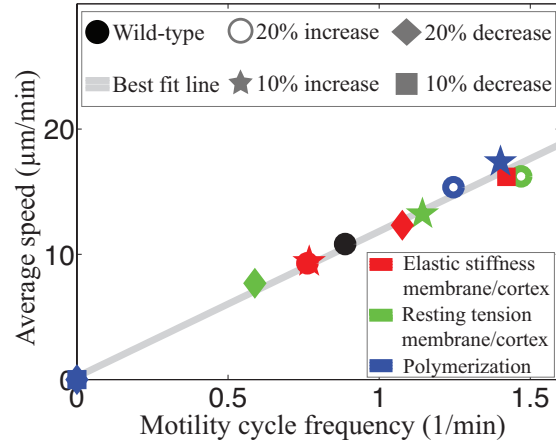
Figure 7: **Cell speed dependence on frequency of motility cycle**. Scatter plot of the average migration speed versus the frequency of the motility cycle for simulated cells with various perturbations to mechanical parameters. The solid line is the least squares fit to the data, $v = 12f$.

of the resting tension in the model weakens the transmission of leading edge forces to rupture back adhesions, resulting in immobility. Similarly, lowering the leading edge forces inhibits migration since the driving forces need to be large enough to overcome adhesion to the surface. In supplementary material S5, we show that decreasing either the threshold rupture load (F_{critical}) or the pseudopod attachment length ($L_{\text{pseudopod}}$) parameter from its baseline value results in a smaller stride length.

Phase diagram of emergent migration modes

Next, we performed a series of simulations to establish how the adhesion parameters affect migration in our model. The cell mechanical parameters are held constant and two adhesion parameters are varied: the surface binding site density, η_0, and the threshold rupture force, F_{critical}. By simultaneously varying these two adhesion parameters, we obtain contour plots of the mean cell speed (Fig. 8). In the two-dimensional parameter-space exploration, we visually identified three emergent motility modes based on the time-evolution of cell length: (1) a gliding mode characterized by oscillations with average amplitude less than 2 μm, (2) a stepping mode characterized by oscillations with average amplitude between 5-8 μm, and lastly, (3) a stationary mode characterized by an average migration speed below 2 μm/min. Based on this classification, we constructed a phase diagram of migration modes on top of the contour plots of average cell speed (Fig. 8).

To mimic biological experiments with different substrate coatings, we consider the resulting motion due to variations only in the surface binding site density (Fig. 8 (a)-(d), supplementary material, Movie S3). At low binding site density, the cell cannot initiate a motility cycle since the low bond formation prevents pseudopod attachment to the surface. When the binding site density is increased, the cell shows gliding-like motility with small length changes and traction stresses similar to Fig. 3A, in particular no evidence of recycling of adhesion sites. As the surface binding site density is further increased, we observe a switch in the motility mode from gliding to stepping. The mean cell speed decreases, the amplitude of the oscillations in length increases, and patterns of stationary and recycled adhesion sites emerge in the kymograph of axial stresses. When binding site density is further elevated, the cell cannot overcome adhesion forces in order to rupture back adhesions and the cell is stuck to the surface. The transition in motility modes from gliding to stepping to stationary reflects the competition between the elastic response of the cell and the cell-substrate adhesion. In the fast motility mode (i.e., gliding), the cell crawls using short-lived adhesions that do not exhibit force-sensitivity, but when adhesion forces are considerably stronger, the cell cannot rupture adhesions and remains stuck to the surface.

Step-like locomotion emerges when the adhesion parameters are in a range similar to the strength of the elastic response. Similar transitions can be obtained by varying the other adhesion parameters.

Our model predicts that gliding motility occurs when adhesions are weakened (bottom left corner in Fig. 8). Since we cannot perform experiments with different ligand concentration, we analyzed experiments with talin A-null *Dictyostelium* cells. Talin A is an actin-binding cytoskeletal protein capable of anchoring the actin cytoskeleton to adhesion proteins [38]. While in animal cells talin constructs and regulates focal adhesions, in *Dictyostelium* it may be involved in the control of motility as defects in cell-surface interaction are observed in moving cells [39, 40]. Preliminary data shows that talin A-null cells move faster and with smaller length changes than wild-type cells (supplementary material Fig. S7) which suggests these cells glide. This experimental result is similar to our model prediction that *Dictyostelium* cells establishing weaker cell-surface interaction employ a gliding-like motility mode.
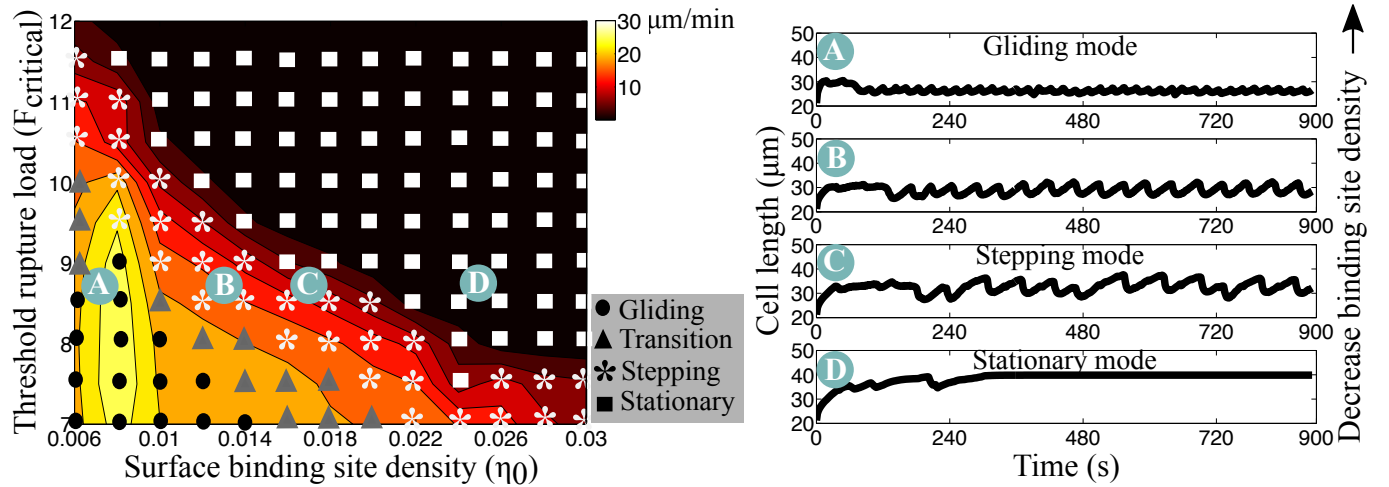

Figure 8: **Simulated average cell speed as a function of two adhesion parameters**. Cell migration speed is reported as a function of two adhesion parameters: threshold rupture load ($F_{critical}$) and surface binding site density (η_0). The symbols indicate the emergent migratory modes: circle, gliding mode, stars, stepping mode, and square, stationary mode (speed below 2 μm/min). Triangles indicate transition between gliding and stepping modes. For a fixed threshold rupture load, $F_{critical} = 8.5$ a.u., we vary the surface binding site density and report the cell length over time in panels (A)-(D). The surface binding site density is (A) $\eta_0 = 0.006$ (gliding mode), (B) $\eta_0 = 0.012$ (transition), (C) $\eta_0 = 0.016$ (stepping mode), (D) $\eta_0 = 0.024$ (stationary).

Discussion

The existing paradigm for the locomotion of *Dictyostelium*, a model organism of amoeboid motility, has been proposed to be the result of complex biochemical and biophysical processes coupled to biomechanics [3]. Here, we show that a simple mechanochemical model could explain the observed phenomena of amoeboid motility: periodic morphological changes, the spatiotemporal dynamics of 3D traction stresses, adhesive sites that are fixed on the surface and recycled through a motility cycle, and the emergent step-like locomotion with preserved stride length across mechanical perturbations. To capture all of these complex, highly-synchronized features, we needed to incorporate the mechanical response of the membrane and cortex, force-sensitive actin-driven polymerization, and force-sensitive interaction with the surface. Despite the coarseness of our simple model, perturbations to the mechanical model parameters impact the frequency of the motility cycle and the migration speed consistent with experiments. In particular, simulated cells perturbed from baseline parameters

continue to crawl in a step-wise manner by conserving the stride length. We further find that the mode of the movement could evolve in response to surface properties: for small availability of surface binding site, cells use a gliding mode with small amplitude oscillations in length, a stepping mode is found at intermediate binding site density; a stationary mode is observed when the availability of binding sites is too large. The three behaviors have been observed in experiments of motile *Dictyostelium* cells but here we show that cells mediate the transition from one mode to another in response to properties of the environment. Further, we find that the migration of talin A-null cells, that display weak anchoring between adhesions and cytoskeleton, is consistent with our model prediction for low surface binding site density. We also find that a gliding motion is exhibited by simulated cells with cell-substrate adhesion modeled by only slip bonds with a sharp rupture threshold (shown in Fig. 3A). This model result is also observed in *Dictyostelium* cells with enhanced nonspecific adhesion, such as on poly-L-lysine coated surfaces (supplementary material, Fig. S6).

Three mechanisms have been proposed to contribute to amoeboid cell migration: actin polymerization, myosin-mediated contraction, and force from osmotic pressure [3]. Our model includes force-dependent polymerization at the leading edge, and pressure which ensures volume conservation but does not drive motility. Contraction enters our model through resting tension in the membrane-cortex but is not coordinated explicitly. While it has been suggested that myosin II motor proteins mediate the contraction phase, myosin II-deficient *Dictyostelium* cells continue to employ cyclic oscillations between extension and retraction phases [15, 41, 42]. This suggests that perhaps a different machinery might be responsible for the coordinated rupture of rear adhesions. Here, we explore this hypothesis by including neither a contraction at the cell rear due to myosin II motors nor a biochemical synchronization between the cell front and rear. We find that the front-to-back communication could be achieved through the mechanics of the membrane-cortex structure only. The polymerization forces at the leading edge cause the cell to deform and thus, exert pulling forces on the cell-substrate adhesions at the rear. Further, we observe that simulated cells with weakened tension continue to crawl but with a slower speed and a longer period of migration (Fig. 7). While this does resemble the behavior reported in myosin II null cells (Fig. 1D), myosin II motors serve multiple functions including contraction and actin crosslinking and thus direct comparison between our mechanical perturbation to tension and myosin II null cells is difficult. Slower locomotion is also experimentally reported with decreases in polymerization activity. *Dictyostelium* cells lacking the SCAR protein, an up-regulator of the branched F-actin nucleation complex Arp2/3 [43], exhibit decreased dendritic polymerization of F-actin at the cell front [42]. These mutant cells undergo motility cycles of decreased frequency and have slower migration speeds (Fig. 1D). This observation is consistent with variations in the rate of polymerization parameter, ρ_1, in the model (Fig. 7).

Our model highlights the necessary components for amoeboid locomotion and their spatiotemporal coordination through mechanics. The effects of biochemical signaling and myosin-mediated contraction at the cell rear may be important for other biological functions, but we find that those are not required to produce amoeboid motility in our model. Recently, other models have highlighted the relevance of mechanics alongside biochemistry in understanding cellular processes. The model in [44] demonstrates that a simple model incorporating stick-slip adhesions and contractile forces is sufficient to capture the emergence of periodic lamellipodial contractions. Another model coupled actin retrograde flow with interaction with the substrate to reveal the mechanism of how a cell is able to sense and respond to the physical properties of the local environment [22]. Here, we contribute to this line of work by illustrating how the mechanical cellular components achieve coordination at the cellular level to give rise to periodic oscillations in cell length and stepping locomotion observed in crawling amoeboid cells.

One emergent characteristic of our model is the localization of tangential traction stresses and adhesions and their apparent spatial recycling seen by the horizontal patches in kymographs. However, we do differ from experiments in that during any particular phase of the motility cycle we have three or four distinct adhesion sites rather than the two or three as reported experimentally. We attribute this difference to the simplified model of the actin cytoskeleton; in our formulation, the cytoskeleton transmits the leading edge forces to the surface on the entire region of contact. A more detailed spatial model of the transmission of forces in the cytoskeleton would not change the main results of this work, specifically the emergent cycles of morphological extension

and retraction, distribution of 3D traction forces, or spatiotemporal adhesion patterns from a mechanosensitive cell-surface interaction. Similar results are also observed with a gradual slip response rather than the sharp threshold response we presented originally in Eq. 4 (supplementary material, S6).

Any form of cell locomotion must rely on the interaction of the cell with the surface to enable pseudopod extension and retraction of the cell rear, and in *Dictyostelium* the molecular basis for this interaction is unknown. Specifically, the *Dictyostelium* genome does not carry genes for integrins or any of the other extracellular matrix proteins [45]. There has been evidence to suggest that actin foci act as the active 'feet' of *Dictyostelium* [8]. Actin foci are dynamic structures localized at the ventral surface of cells and are coordinated with the repetitive cycles of morphological extension and retraction that occur during migration. Interestingly, the foci are fixed on the surface during migration and are found in regions where significant traction forces are exerted on the substratum [8]. Our force-sensitive description of cell-substrate interaction is consistent with the existing hypothesis about actin-foci 'feet'. While our prediction does not imply a specific adhesion complex, we propose that this interaction must have a force-sensitive response to produce the reported spatiotemporal dynamics of traction stresses and the periodic cycles of morphological changes. Although the role of specific adhesion versus nonspecific adhesion in *Dictyostelium* is still unclear [45], altering mechanosensing in these cells has been shown to be important in adhesion to the substrate and migration speed [46]. Our work suggests that amoeboid motility shares many key features with the motility of higher eukaryotic cells, including for example, the formation of catch bond adhesions seen in integrins. It remains to be seen whether this mechanosensitive interaction with the surrounding is also the underlying mechanism for the experimental observations of a bimodal relationship between motility speed and the stiffness of the extracellular matrix for 3D amoeboid migration.

Author Contributions

C.C., J.C.d.Á., and R.D.G. designed the project. C.C., S.W., R.D.G. developed model with input from A.M.. C.C. performed and analyzed the computer simulations. J.C.d.Á. and E.B. performed and analyzed the biological experiments.

Acknowledgments

References

[1] Lauffenburger, D. A., and A. F. Horwitz, 1996. Cell migration: a physically integrated molecular process. *Cell.* 84:359–369.

[2] Bailly, M., and J. Condeelis, 2002. Cell motility: insights from the backstage. *Nat. Cell Biol.* 4:E292–294.

[3] Friedl, P., S. Borgmann, and E. B. Brocker, 2001. Amoeboid leukocyte crawling through extracellular matrix: lessons from the *Dictyostelium* paradigm of cell movement. *J. Leukocyte Biol.* 70:491–509.

[4] Devreotes, P. N., and S. H. Zigmond, 1988. Chemotaxis in eukaryotic cells: a focus on leukocytes and *Dictyostelium. Annu. Rev. Cell Biol.* 4:649–686.

[5] Stossel, T. P., 1994. The machinery of blood cell movements. *Blood.* 84:367–379.

[6] Kessin, R. H., 2001. *Dictyostelium*: Evolution, Cell Biology, and the Development of Multicellularity. Cambridge University Press, Cambridge, first edition.

[7] Friedl, P., and K. Wolf, 2003. Tumour-cell invasion and migration: diversity and escape mechanisms. *Nat. Rev. Cancer.* 3:362–374.

[8] Uchida, K. S., and S. Yumura, 2004. Dynamics of novel feet of *Dictyostelium* cells during migration. *J. Cell Sci.* 117:1443–1455.

[9] Lombardi, M. L., D. A. Knecht, M. Dembo, and J. Lee, 2007. Traction force microscopy in *Dictyostelium* reveals distinct roles for myosin II motor and actin-crosslinking activity in polarized cell movement. *J. Cell Sci.* 120:1624–1634.

[10] Meili, R., A.-L. Baldomero, J. C. del Álamo, R. A. Firtel, and J. C. Lasheras, 2010. Myosin II is essential for the spatiotemporal organization of traction forces during cell motility. *Mol. Biol. Cell.* 21:405–417.

[11] Titus, M. A., 2004. The role of talin and myosin VII in adhesionA FERM connection. *In* A. Ridley, M. Peckham, and P. Clark, editors, Cell Motility: From Molecules to Organisms, John Wiley & Sons, Chichester, England.

[12] Bastounis, E., R. Meili, B. Álvarez-González, J. Francois, J. C. del Álamo, R. A. Firtel, and J. C. Lasheras, 2014. Both contractile axial and lateral traction force dynamics drive. *J. Cell Biol.* 204:1045–1061.

[13] Hall, A., 1998. GTPases and the actin cytoskeleton. *Science.* 279:509–514.

[14] Parent, C. A., and P. N. Devreotes, 1999. A cell's sense of direction. *Science.* 284:765–770.

[15] Yumura, S., and T. Kitanishi-Yumura, 1990. Fluorescence-mediated visualization of actin and myosin filaments in the contractile membrane-cytoskeleton complex of *Dictyostelium discoideum. Cell Struct. Funct.* 15:355–364.

[16] Álvarez-González, B., R. Meili, E. Bastounis, R. A. Firtel, J. C. Lasheras, and J. C. del Álamo, 2015. Three-dimensional balance of cortical tension and axial contractility enables fast amoeboid migration. *Biophys. J.* 108:1–12.

[17] Yamada, K. M., and B. Geiger, 1997. Molecular interactions in cell adhesion complexes. *Curr. Opin. Cell Biol.* 9:76–85.

[18] Renkawitz, J., K. Schumann, M. Weber, T. Lämmermann, H. Pflicke, M. Piel, J. Polleux, J. Spatz, and M. Sixt, 2009. Adaptive force transmission in amoeboid cell migration. *Nat. Cell Biol.* 11:1438–1443.

[19] del Álamo, J. C., R. Meili, B. Alonso-Latorre, J. Rodríguez-Rodríguez, A. Aliseda, R. A. Firtel, and J. C. Lasheras, 2007. Spatio-temporal analysis of eukaryotic cell motility by improved force cytometry. *Proc. Natl. Acad. Sci. USA.* 104:13343–13348.

[20] DiMilla, P. A., K. Barbee, and D. A. Lauffenburger, 1991. Mathematical model for the effects of adhesion and mechanics on cell migration speed. *Biophys J.* 60:15–37.

[21] Mogilner, A., and G. Oster, 1996. Cell motility driven by actin polymerization. *Biophys J.* 71:3030–3045.

[22] Chan, C. E., and D. J. Odde, 2008. Traction dynamics of filopodia on compliant substrates. *Science.* 322:1687–1691.

[23] Walcott, S., and S. X. Sun, 2010. A mechanical model of actin stress fiber formation and substrate elasticity sensing in adherent cells. *Proc. Natl. Acad. Sci. USA.* 107:77577762.

[24] Evans, E. A., 1983. Bending elastic modulus of red blood cell membrane derived from buckling instability in micropipet aspiration tests. *Biophys. J.* 43:27–30.

[25] John, K., D. Caillerie, P. Peyla, A. Raoult, and C. Misbah, 2013. Nonlinear elasticity of cross-linked networks. *Phys. Rev. E.* 87:042721.

[26] Parekh, S. H., O. Chaudhuri, J. A. Theriot, and D. A. Fletcher, 2005. Loading history determines the velocity of actin-network growth. *Nat. Cell Biol.* 7:1219–1223.

[27] Prass, M., K. Jacobson, A. Mogilner, and M. Radmacher, 2006. Direct measurement of the lamellipodial protrusive force in a migrating cell. *J. Cell Biol.* 174:767–772.

[28] Heinemann, F., H. Doschke, and M. Radmacher, 2011. Keratocyte lamellipodial protrusion is characterized by a concave force-velocity relation. *Biophys. J.* 100:1420–1427.

[29] Cox, D., J. A. Ridsdale, and J. Hartwig, 1995. Genetic deletion of ABP-120 alters the three-dimensional organization of actin filaments in *Dictyostelium* pseudopods. *J. Cell Biol.* 128:819–835.

[30] Wessels, D., H. Vawter-Hugart, J. Murray, and D. R. Soll, 1994. Three-dimensional dynamics of pseudopod formation and the regulation of turning during the motility cycle of *Dictyostelium*. *Cell Motil. Cytoskel.* 27:1–12.

[31] Edwards, C. M., and U. S. Schwarz, 2011. Force localization in contracting cell layers. *Phys. Rev. Lett.* 107:128101.

[32] Oakes, P. W., S. Banerjee, C. M. Marchetti, and M. L. Gardel, 2014. Geometry regulates traction stresses in adherent cells. *Biophys. J.* 107:825–833.

[33] Iwadate, Y., and S. Yumura, 2008. Actin-based propulsive forces and myosin-II-based contractile forces in migrating *Dictyostelium* cells. *J. Cell Sci.* 121:1314–1324.

[34] Bell, G. I., 1978. Models for the specific adhesion of cells to cells. *Science.* 200:618.

[35] Kong, F., A. J. Garcia, A. P. Mould, M. J. Humphries, and C. Zhu, 2009. Demonstration of catch bonds between an integrin and its ligand. *J. Cell Biol.* 185:1275–1284.

[36] Rakshita, S., Y. Zhang, K. Maniboda, O. Shafraza, and S. Sivasankar, 2012. Ideal, catch, and slip bonds in cadherin adhesion. *Proc. Natl. Acad. Sci. USA.* 109:18815.

[37] Novikova, E. A., and C. Storm, 2013. Contractile fibers and catch-bond clusters: a biological force sensor? *Biophys. J.* 105:1336–1345.

[38] Cornillon, S., L. Gebbie, M. Benghezal, P. Nair, S. Keller, B. Wehrle-Haller, F. B. S. J. Charette, F. Letourneur, and P. Cosson, 2006. An adhesion molecule in free-living *Dictyostelium* amoebae with integrin β features. *EMBO Rep.* 7:617–621.

[39] Niewöhner, J., I. Weber, M. Maniak, A. Müller-Taubenberger, and G. Gerisch, 1997. Talin-null cells of *Dictyostelium* are strongly defective in adhesion to particle and substrate surfaces and slightly impaired in cytokinesis. *J. Cell Biol.* 138:349–361.

[40] Masatsune, T., K. Yoshida, A. Nagasaki, S. Yonemura, A. Muller-Taubenberger, and T. Q. P. Uyeda, 2008. Overlapping functions of the two talin homologues in *Dictyostelium*. *Eukaryot. Cell.* 7:906–916.

[41] Uchida, K. S., T. Kitanishi-Yumura, and S. Yumura, 2003. Myosin II contributes to the posterior contraction and the anterior extension during the retraction phase in migrating *Dictyostelium* cells. *J. Cell Sci.* 116:51–60.

[42] Bastounis, E., R. Meili, B. Alonso-Latorre, J. C. del Álamo, J. C. Lasheras, and R. A. Firtel, 2011. The SCAR/WAVE complex is necessary for proper regulation of traction stresses during amoeboid motility. *Mol. Biol. Cell.* 22:3995–4003.

[43] Blagg, S. L., and R. H. Insall, 2004. Solving the WAVE function. *Nat. Cell Biol.* 6:279–281.

[44] Wolgemuth, C. W., 2005. Lamellipodial contractions during crawling and spreading. *Biophys J.* 89:1643–1649.

[45] Loomis, W. F., D. Fuller, E. Gutierrez, A. Groisman, and W. J. Rappel, 2012. Innate non-specific cell substratum adhesion. *PLoS ONE.* 7:e42033.

[46] Zhu, X., R. Bouffanais, and D. K. P. Yue, 2015. Interplay between motility and cell-substratum adhesion in amoeboid cells. *Biomicrofluidics* 9:e054112.

Supplementary Material

S.1   Experimental materials and methods

The experimental protocols used to culture *Dictyostelium* cells and quantify the mechanics of their chemotactic migration were described at length in our previous studies [1–5]. The key steps of these protocols are summarized below.

Cell culture and microscopy. *Dictyostelium discoideum* cells were grown under axenic conditions in HL5 growth medium in tissue culture plates. This study reports on six different cell lines: wild type Ax2 and Ax3, myosin II null, myosin II essential light chain null, scrA null, and talin A-null cells. All the cell lines were obtained from the Dicty Stock Center, except for the talin null cells which were a gift from M. A. Titus (University of Minnesota, Minneapolis, MN). Aggregation competent cells were prepared by pulsing 5×10^6 cells/ml suspension in Na/K phosphate buffer (9.6 mM KH2PO4, 2.4 mM Na2HPO4, pH 6.3) with cAMP to a concentration of 30 nM every 6 minutes for 6 hours. Cells were seeded onto the functionalized polyacrylamide substrate and allowed to adhere. A drawn glass capillary mounted on a micromanipulator served as the source of chemoattractant (150 mM cAMP in an Eppendorf femtotip, Eppendorf, Germany). To identify the cell contours, differential interference contrast (DIC) images were acquired using a 40X air objective. A custom algorithm using MATLAB (Mathworks Inc., Natick, MA) identified the contour of the cells [6].

Polyacrylamide gel preparation. We fabricated 12-mm diameter, $\sim$40 μm-thick polyacrylamide gels of 4% acrylamide and 0.056% bisacrylamide ($\sim$900 Pa [7]) on 22-mm square #1 glass coverslips [8, 9]. We mounted the coverslips with the gels in Petri dishes with a circular opening in the bottom using silicon grease (Dow Corning, Midland, MI). Our gels consist of two layers: the bottom layer contains no beads, and the upper one contains 0.04% carboxylate modified red latex beads of 0.1 μm diameter (FluoSpheres; Molecular Probes, Eugene, OR). We made the gels physiologically compatible by crosslinking collagen I to the surface of the polyacrylamide. We used 1 mM Sulfo-SANPAH (Thermo Sci., Rockford, IL) after UV activation to crosslink 0.25 mg/ml collagen I. To test the effect of increased substratum adherence, 20 mg/ml of poly-L-Lys (MW=30000-70000, P9155 Sigma-Aldrich) were mixed together with the collagen solution, while the remaining protocol steps were the same as described above. Different concentrations of poly-L-lysine were tested, and the one selected was chosen since wild-type cells were still able to chemotax, but with deeply decreased speed. The gels were incubated overnight at room temperature. After washing, the gels were stored in Na/K phosphate buffer (9.6 mM KH2PO4, 2.4 mM Na2HPO4, pH 6.3, same composition as used in the experiments) and antibiotic (40 μM Ampicillin) for up to a week.

Three-dimensional force microscopy (3DFM). We imaged z-stacks containing fluorescent beads, consisting of 24 planes separated 0.4 μm from each other and acquired images every 5 seconds. The 3D substrate deformation was determined for each z-stack via image cross-correlation with a non-deformed reference z-stack, which was obtained after the cell moved out of the field of view. Both instantaneous and reference z-stacks were divided into 3D interrogation boxes of size $24 \times 24 \times 24$ pixels to balance resolution and signal-to-noise while minimizing phototoxic effects. These settings provided a Nyquist spatial resolution of 2.1 μm. Using the measured deformations as boundary conditions, we computed the three-dimensional stresses generated by the cells on the substrate using the 3D Green's function of the elastic equation given by del Álamo et al. [10].

S.2   The full model equations

In our two-dimensional model the cell is crawling in the horizontal direction with surface attachments between the cell and the surface below it. The cell membrane and its underlying cortex are represented as one structure

with position $\boldsymbol{X}(s,t) = (x(s,t), y(s,t))$ where t is time and s is a local parametric coordinate on the structure. Here, $\widehat{x}$ is a unit vector in the horizontal direction of crawling while $\widehat{y}$ is in the vertical direction. The system is described by the following force-balance equation:

$$\xi \frac{\partial \boldsymbol{X}}{\partial t} = \boldsymbol{F}_{\text{membrane/cortex}} + \boldsymbol{F}_{\text{pressure}} + \boldsymbol{F}_{\text{polymerization}} + \boldsymbol{F}_{\text{cytoskeleton}} + \boldsymbol{F}_{\text{surface}} . \tag{S1}$$

The cell experiences a velocity-dependent drag with the environment where ξ denotes the viscous drag coefficient. Below, we present the constitutive laws for the forces in the force-balance equation.

- The elastic response of the membrane/cortex structure:

$$\boldsymbol{F}_{\text{membrane/cortex}} = \frac{\partial}{\partial s} \left[\left(\gamma + k(|\partial \boldsymbol{X}/\partial s| - 1) \right) \widehat{\tau} \right] \tag{S2}$$

where γ is the resting tension and k is the stiffness of the material. The tangent vector to the curve $\boldsymbol{X}(s,t)$ is defined as $\widehat{\tau} = \partial_s \boldsymbol{X}/|\partial_s \boldsymbol{X}|$ where $\partial_s \boldsymbol{X} = \partial \boldsymbol{X}/\partial s$.

- The cytosol is modeled as a viscous medium and is assumed to have a resting internal pressure p_0 and resting volume V_0. The intracellular pressure force is given by,

$$\boldsymbol{F}_{\text{pressure}} = \left(p_0 + \kappa_{\text{cell}} \ln(V/V_0) \right) \widehat{n} . \tag{S3}$$

Here, κ_{cell} represents the bulk modulus and the normal vector to the curve $\boldsymbol{X}(s,t)$ is given by $\widehat{n} = \partial_s \widehat{\tau}/|\partial_s \widehat{\tau}|$ where $\widehat{\tau}$ is the tangent vector defined above. A flow is volume preserving if $\iint_\Omega \nabla \cdot \boldsymbol{u} \, dA = \int_{\partial\Omega} \boldsymbol{u} \cdot \widehat{n} \, ds = 0$ where Ω denotes the interior domain, while $\partial\Omega$ is its boundary. The membrane velocity is given by Eq. S1 and so this condition is met by requiring $\int \boldsymbol{F} \cdot \widehat{n} \, ds = \xi \int \boldsymbol{u} \cdot \widehat{n} \, ds = 0$, where $\boldsymbol{F}$ denotes the sum of the forces from Eq. S1. Thus, the resting pressure is computed by,

$$\int \left(\boldsymbol{F}_{\text{pressure}} + \boldsymbol{F}_{\text{remaining}} \right) \cdot \widehat{n} \, ds = 0$$

$$\int \left(p_0 \, \widehat{n} + \boldsymbol{F}_{\text{remaining}} \right) \cdot \widehat{n} \, ds = 0$$

$$p_0 \int ds + \int \boldsymbol{F}_{\text{remaining}} \cdot \widehat{n} \, ds = 0$$

$$p_0 = - \frac{\int \boldsymbol{F}_{\text{remaining}} \cdot \widehat{n} \, ds}{\int ds} .$$

Here, $\boldsymbol{F}_{\text{remaining}}$ represents all of the other forces involved in the force balance in Eq. S1. If the equation was solved analytically, this pressure force due to the resting internal pressure would be sufficient to enforce volume conservation. Due to numerical time integration errors, an additional volumetric correction term is introduced to further ensure volume conservation is maintained throughout the simulation.

- The force-velocity relationship for the branching of actin filaments at the leading edge is described by relations of the form, $v = v(F_L)$, where F_L is the force against the protrusion. We assume the following one-dimensional model for the leading edge velocity due to polymerization against the cell membrane,

$$v = \rho_1 \, e^{-\rho_2 F_L} + \rho_3 . \tag{S4}$$

Force-velocity relations of this form were observed theoretically [16] and experimentally in a certain region of the load forces [17–19]. The constants $\rho_{1,2,3}$ can be determined experimentally through measurements of the force-velocity relationship in directional polymerization of F-actin filaments. An equivalent way to formulate this relation is to assume the polymerization force is a function of the protrusion rate:

$F_{\text{polymerization}} = F_{\text{polymerization}}(v)$. Then, the force-balance equation in the direction of motion (Eq. S1) at the cell front has the form:

$$F_{\text{polymerization}}(v) + F_L = \xi v \, . \tag{S5}$$

To implement the one-dimensional polymerization model in Eq. S5, the force acting against the protrusion, F_L, is computed as a spatial average of the forces acting on the membrane-cortex structure in the region of polymerization. At the cell front, there is no interaction between the membrane-cortex structure and the substrate, and therefore $F_{\text{surface}} = 0$ and $F_{\text{cytoskeleton}} = 0$. Thus, the force against the protrusion is given by the average of the remaining forces at the cell front,

$$F_L = \frac{\int_{\mathcal{P}} \left| \boldsymbol{F}_{\text{membrane/cortex}} + \boldsymbol{F}_{\text{pressure}} \right| ds}{\int_{\mathcal{P}} ds} \, . \tag{S6}$$

Given this expression for the 'load' force and the polymerization model described in Eqs. S4 and S5, we can solve for an effective driving force, $F_{\text{polymerization}}$, at the leading edge only in the direction of motion. Note that this choice of $F_{\text{polymerization}}$ ensures that the cell front moves with the velocity given in Eq. S4 in the horizontal direction. Using our simulation parameters provided in Table S.1, the effective force-velocity relation at the cell front is shown in Fig. S1.
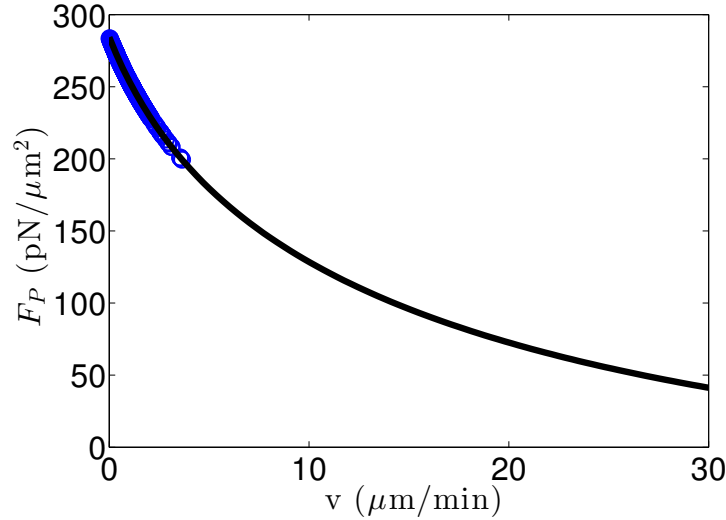

Figure S1: The effective polymerization force-velocity relation at the leading edge. The circles represent the region of velocities and forces in which the simulated cell operates based on the parameters presented in Table S.1 (and also the same parameters used to generate the results in Fig. 6). As the load force increases, the cell front velocity will decrease eventually to zero when the leading edge stalls at a force density of 283 pN/μm^2. Stall force of this order of magnitude was experimentally measured [16, 18] and it corresponds to a stall force per filament in the range of $\sim$1-10 pN predicted and observed in multiple studies.

- The action of cytoskeleton is to transmit the leading edge polymerization forces to the underlying surface. The protrusive forces at the leading edge are integrated over the region of polymerization and distributed uniformly to the region of cell-surface contact to ensure zero sum of polymerization and cytoskeletal forces,

$$\boldsymbol{F}_{\text{cytoskeleton}} = -\frac{\int_{\mathcal{P}} |\boldsymbol{F}_{\text{polymerization}}| \, ds}{\int_{\mathcal{C}} ds} \, \widehat{x} \, . \tag{S7}$$

The membrane-cortex structure is within the region of contact, $\mathcal{C}$, if it is within 5 μm of the surface in the vertical direction.

- We assume the cell crawls on top of a flat surface at along the horizontal axis ($y = 0$). The interaction between the cell and the underlying surface is given through both physical adhesive connections and a repulsive force due to contact with the surface:

$$\boldsymbol{F}_{\text{surface}} = \boldsymbol{F}_{\text{steric}} + \boldsymbol{F}_{\text{adhesion}} . \tag{S8}$$

  ○ Below a certain distance, δ_w, the cell feels a nonspecific steric force of the form:

$$\boldsymbol{F}_{\text{steric}} = -k_{\text{steric}}\left(|y(s,t)| - \delta_w\right)\widehat{y} \tag{S9}$$

  and is zero otherwise. Here, k_{steric} represents the stiffness of this steric interaction.

  ○ The adhesive force is

$$\boldsymbol{F}_{\text{adhesion}} = \begin{cases} \zeta N(t,s)(|\boldsymbol{X} - \boldsymbol{X}_{\text{surface}}|/\ell_0 - 1)\frac{\boldsymbol{X}-\boldsymbol{X}_{\text{surface}}}{|\boldsymbol{X}-\boldsymbol{X}_{\text{surface}}|} & \text{if } \frac{|\boldsymbol{F}_{\text{adhesion}}|}{N} < F_{\text{critical}} \\ 0 & \text{otherwise.} \end{cases} \tag{S10}$$

At each binding site, the adhesive force is the result of the local bond density per adhesion site, $N(t,s)$, a constant adhesive stiffness, ζ, and the elastic deformation of the bond from its resting length, ℓ_0. Locations of binding along the surface are denoted by $\boldsymbol{X}_{\text{surface}}$. The position of $\boldsymbol{X}_{\text{surface}}$ is determined per bond during bond formation; when an adhesive bond forms it binds to the surface directly below the membrane-cortex structure. For the lifetime of the bond, the binding position remains fixed along the surface. The local bond density can vary between zero to full occupancy, $0 \le N(t,s) \le 1$.

For the adhesive force, three models are considered for local bond density per adhesion site, $N(t,s)$:

(1) Uniform slip bonds: $N(t,s) = N = 1$ throughout time and over the entire region of cell-surface contact;

(2) Non-uniform slip bonds: $N(t,s) = N$ throughout time with

$$N = \begin{cases} 1 & \text{in the region of contact within 6 } \mu\text{m near the cell front and rear} \\ 0 & \text{otherwise;} \end{cases}$$

(3) Uniform catch/slip bonds: $\partial N(t,s)/\partial t = k^+\eta_0(1 - N) - k^- N \exp\left(-\frac{\alpha|\boldsymbol{F}|/N}{k_B T}\right)$. where k^+ is a constant binding rate, η_0 is the unsaturated substrate ligand concentration, k^- is the zero-force unbinding rate, and α is a microscopic length scale characterizing the unbinding transition.

Bond rupture: A bond can break at any spatial or temporal location when the adhesive force per bond exceed a critical threshold load, F_{critical}.

Bond formation: The pseudopod is prevented from interaction with the surface until it reaches a minimal critical length, $L_{\text{pseudopod}}$. Once the length condition is met, proximity to the surface determines if bonds form between the pseudopod and the substrate. In the first two models for bond density, a bond forms with $N = 1$, while in the third model, the initial bond density per site is $N = (k^+\eta_0)\Delta t$ where Δt is the numerical time step.

Discretization of the model

To simulate the dynamics of a crawling cell, the membrane-cortex structure is spatially discretized using 162 points and every discrete point has its own position and velocity field. The temporal discretization is $\Delta t =$

1.788×10^{-4} seconds and the averaged spatial discretization is $\Delta s = 0.4\,\mu$m. Every time instance, local forces are computed at every discretized point along the membrane-cortex structure and its position is updated according to the local force balance described in Eq. S1. A first order finite difference scheme is used to evaluate spatial derivatives. Forward Euler method is used to evolve the force balance equation at each point on the structure. The cell achieves an equilibrated shape before migration is initiated. Model parameters are provided in supplementary material, Table S1.

S.3 Model parameters

We perform simulations using the baseline parameter values listed in Table S1. Where possible, parameter values are chosen to be roughly the same order of magnitude as measured or estimated values in literature. However, some model parameters are not experimentally measurable, and below we give a brief dicussion of our estimates of these parameters.

The radius for a spherical *Dictyostelium* in the absence of adhesions to the surface is set in the simulation, $R_0 = 7.56\ \mu$m, in order to yield a crawling cell length of around 20 μm. *Dictyostelium discoideum* amoebas are known to be pressurized due to the contraction of the actomyosin network of the cortex. In our model, the resting tension (γ) in the membrane-cortex structure is mostly composed of the cortical tension. Our value of the resting tension in Table S1. is in good agreement with previous measurements of the cortical tension that reported an approximate value of 1000 pN/μm [5, 11–13]. The measurements were obtained from micropipette aspiration experiments and approximations from Laplace's law with given hydrostatic pressure differential. Without more reliable measurements of the elastic properties of *Dictyostelium* membrane and cortex, we chose the elastic parameter k to be the same as the resting tension so that deformation forces are comparable to forces from tension. For a given set of forces, the drag cofficient determines the resulting crawling velocity and thus, is set to match the timescale of biological motion, $\xi = 72$ pN s/μm^3.

Little is known about the binding receptors in *Dictyostelium*. Although the *Dictyostelium* genome does not carry any genes for integrins, we compare the parameters of the catch bond dynamics model to experimental values for other cell types with integrin-mediated adhesions. In [15], the catch bond between the extracellular matrix component fibronectin (FNIII$_{7-10}$) and the cellular integrin ($\alpha_5\beta_1$) is found to have a zero-force unbinding rate of $k^- = 55s^{-1}$, while the binding rate ranges between $k^+\eta_0 = 1 - 10s^{-1}$.

The coefficients of polymerization force driving pseudopod extension are unspecified for *Dictyostelium*. The values of listed in Table S1 were chosen to overcome the strength of adhesion forces and reproduce migration speeds of approximately the scale observed in the experiments. The minimal length of the pseudopod for attachment was chosen to be consistent with [2, 3, 5, 14] (reported between 6-12 μm).

S.4 Perturbations to mechanical parameters

We performed a series of simulations of cells with perturbations to mechanical parameters by varying the elastic spring constant, k, and resting tension, γ, of the membrane-cortex structure but also the first constant of the polymerization force, ρ_1. The resulting averaged cell speed, period of motility cycle, and cell length are reported below in Table S2. The stride length is computed from the average cell speed and period of motility cycle, $\lambda = V/f$.

S.5 Parameters relevant for stride length in the model

Fig. 7 suggests that cells perturbed from baseline parameters not only use stepping motility but do so by approximately preserving their stride length, $\lambda = 12\ \mu$m. We note that perturbations considered in Fig. 7: the resting tension, the elastic spring constant, and the strength of polymerization (ρ_1), do not alter the stride length

Symbol	Definition	Numerical value
γ	Resting tension for membrane-cortex link	800 pN/μm
k	Elastic stiffness for membrane-cortex link	800 pN/μm
κ_{cell}	Bulk modulus	800 kPa
k_{steric}	Constant for cell-substrate steric interaction	80 kPa
δ_w	Steric separation distance	0.6 μm
ζ	Adhesion site strength	800 pN/μm^2
ℓ_0	Resting spring length	0.4 μm
$k^+\eta_0$	Binding rate	16.1074 s^{-1}
k^-	Zero-force unbinding rate	322.1460 s^{-1}
α	Length scale of unbinding transition	1.25$\times$10$^{-4}\mu m^2$/pN
F_{critical}	Threshold adhesive force	8400 pN/μm^2
$L_{\text{pseudopod}}$	Pseudopod minimal length for attachment	10 μm
ρ_1	Polymerization constant	11.5556 μm/s
ρ_2	Polymerization constant	0.0082 μm^2/pN
ρ_3	Polymerization constant	1.1111 μm/s

Table S1: Definition and values of parameters for crawling simulation.

of the motility cycle. For this exploration, we identify which parameters in our model that could determine this emergent length scale, λ. In particular, we show that the criteria used for pseudopod length for attachment ($L_{\text{pseudopod}}$) and the threshold rupture load in the adhesive force (F_{critical}) are two parameters that can change the stride length in our model (see Fig. S2).

For individual variations of the two parameters, threshold rupture load and pseudopod attachment length, we performed a series of simulations with perturbations to cellular parameters. The mean speed of migration and the frequency of the motility cycle are evaluated for each set of simulations and a stride length is computed through a linear fit, $v = \lambda \cdot f$ (as shown in Fig. S2 B, C). We find that decreasing the threshold rupture load from its baseline value (F^*) or the pseudopod length from its baseline value (L^*) results in smaller stride length (Fig. S2A). For this parameter regime, increasing the threshold rupture load results in no locomotion while increasing the pseudopod length results in a larger stride length. The baseline values for these two parameters are provided in Table S1 (specifically, $F^* = 8400$ pN/μm^2 and $L^* = 10$ μm). Thus, there is a positive relation between the stride length and threshold rupture load per bond but also between the stride length and the pseudopod attachment length.

S.6   A gradual slip response

Instead of a sharp threshold rupture load, $\boldsymbol{F}_{\text{critical}}$, for the slip response of the bond dynamics in Eq. 5, one could model the slip response with a gradual force-sensitivity as described in [15]:

$$\frac{\partial}{\partial t}N(t,s) = k^+\eta_0(1-N) - k_c^- N \exp\left(-\frac{\alpha|\boldsymbol{F}|/N}{k_BT}\right) - k_s^- N \exp\left(\frac{\beta|\boldsymbol{F}|/N}{k_BT}\right). \tag{S11}$$

Here, $k_c^- = k^-$ is the zero-force unbinding rate for the catch response, while k_s^- is the zero-force unbinding rate for the slip response, and β is a microscopic length scale characterizing the unbinding transition for the slip response. We fix the unbinding rate for the slip response, k_s^-, to be an order magnitude smaller than the unbinding rate for the catch response. This ensures that in the low applied force regime, the catch response is the dominant behavior as it was in the previous slip model. The emergent behavior for different values for

Description	Numerical value	Speed (μm/min)	Period (min)	Cell length (μm)	Stride length ($\lambda = V/f$)
Baseline cell		11	1.1	31	12
Tension^{++} mutant	$\gamma = 960$ pN/μm	16	0.7	25	11
Tension^{+} mutant	$\gamma = 880$ pN/μm	13	0.9	28	12
Tension^{-} mutant	$\gamma = 720$ pN/μm	8	1.7	35	13
Tension^{--} mutant	$\gamma = 640$ pN/μm	<2	–	39	–
Elastic stiffness^{++} mutant	$k = 960$ pN/μm	9	1.3	33	12
Elastic stiffness^{+} mutant	$k = 880$ pN/μm	9	1.3	32	12
Elastic stiffness^{-} mutant	$k = 720$ pN/μm	12	0.9	29	11
Elastic stiffness^{--} mutant	$k = 640$ pN/μm	16	0.70	26	11
Polymerization^{++} mutant	$\rho_1 = 1664$ pN/μm^2	17	0.7	32	12
Polymerization^{+} mutant	$\rho_1 = 1248$ pN/μm^2	15	0.8	32	12
Polymerization^{-} mutant	$\rho_1 = 624$ pN/μm^2	5	–	32	–
Polymerization^{--} mutant	$\rho_1 = 416$ pN/μm^2	<2	–	29	–

Table S2: Motility changes due to variations in cell mechanical parameters

the unbinding transition length scale are presented in Fig. S3. Below, we assess the effect of this gradual slip response model on the emergent motility illustrated in Fig. 6.

Simulations with bond dynamics given by Eq. S11 show that depending on the β parameter, all three modes can also be captured by this model: stuck (Fig. S4 B), stepping (Fig. S4 C, D), and gliding (Fig. S4 E). The emergent stepping motility mode is reported by the spatiotemporal patterns of the axial traction stresses and the time evolution of the cell length (Fig. S4 F, G) which quantitatively agree with to those obtained with a sharp slip response in Fig. 6 A, B.

We note that the transition between motility modes with varying the unbinding transition length scale, β, is phenomenologically the same as the transition with threshold rupture load seen through vertical changes in Fig. 8. With a sharp slip response, our model predicted that decreasing the threshold rupture load results in weakened adhesions and a transition to a gliding-like locomotion. A large value for β results in adhesions which rupture with lower applied forces. For these larger values for β is also the regime where gliding-like locomotion is reported in the improved bond dynamics model (see Fig. S3). This result suggests that the catch response and not the slip response of the adhesive bonds is instrumental to capture the observed cyclic oscillations in cell length and the spatiotemporal patterns of the axial traction forces.
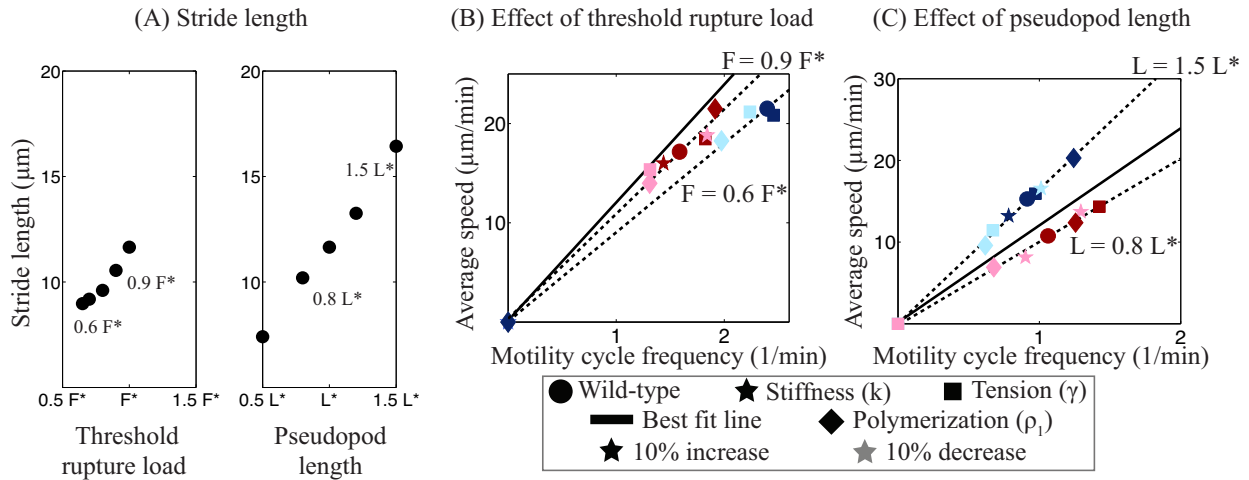
Figure S2: **The threshold rupture load and the length for pseudopod attachment are two parameters that determine the emergent stride length.** (A) The stride length is plotted as a function of both the threshold rupture load per bond and the pseudopod length required for attachment. The stride length is observed to be proportional to either of the two paramaters varied. L^* and F^* denote the baseline values for the two parameters, pseudopod length and critical rupture load, respectively, which are reported in Table S1. (B,C) For two variations of the critical rupture load (B) and two variations of the pseudopod length (C), the mean speed of migration as a function of the frequency of the motility cycle are plotted for cells with perturbations to cellular parameters. The dashed lines are the least squares fit to the data points, while the solid line is the least squares fit for the baseline data replotted from Fig. 7. Darker colors indicate increases from baseline cellular parameters while lighter colors indicate decreases from the baseline parameters.
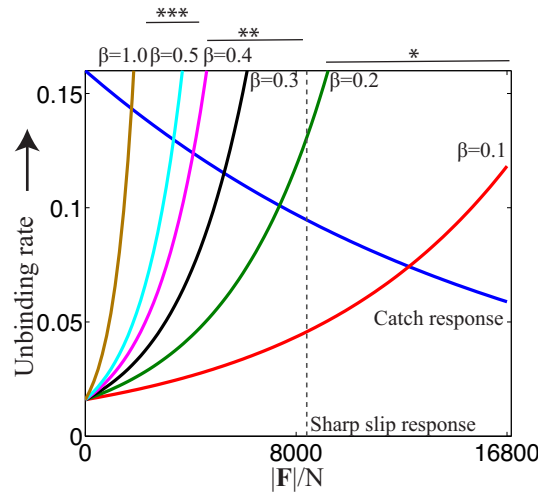

Figure S3: **The unbinding rate of a bond is plotted as a function of the applied force density.** The blue curve denotes the unbinding rate due to the catch response, while the dotted gray line shows the sharp unbinding rate due to the slip response in our model. Instead of a sharp slip response, one could model the slip unbinding rate with varying gradual response curves: $\beta = 0.1, 0.2, 0.3, 0.4, 0.5, 1$. For low values of the β parameter, the cell is stuck to the surface and cannot overcome adhesive forces ($*$), and as the β parameter is increased, stepping motility emerges ($**$). For even larger values of β, the cell is seen to undergo small amplitude length oscillations indicative of gliding motility mode ($***$).
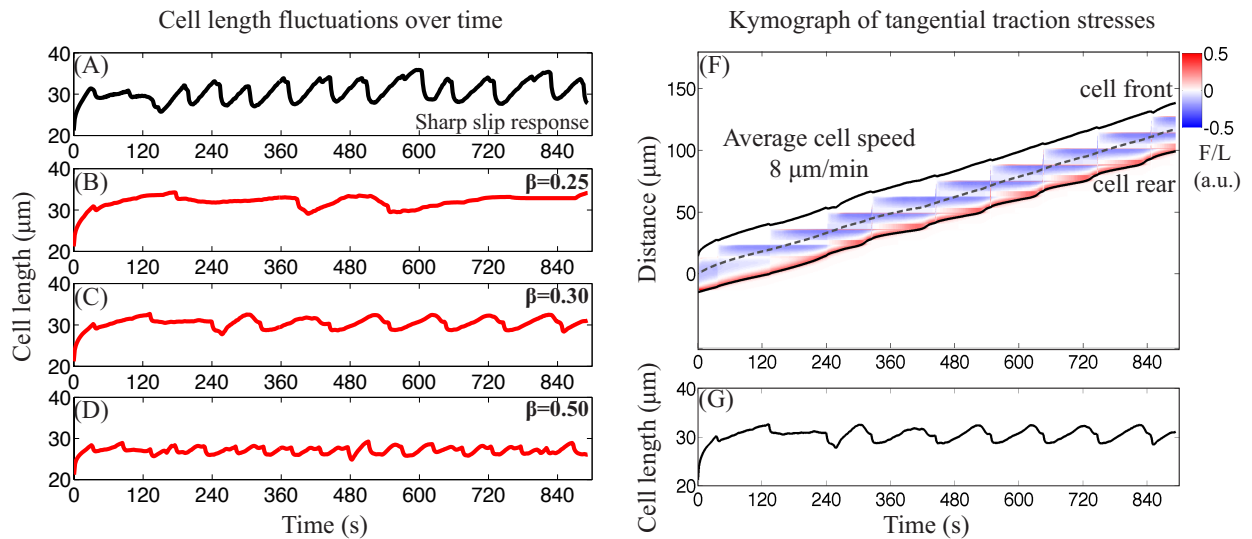
Figure S4: **All three amoeboid motility modes emerge in a model of bond dynamics with a gradual slip response.** For various slip response in bond dynamics, the cell length over time is reported in panels (A)-(D). The cyclic length oscillations reported in the paper with a sharp slip response are reproduced for comparison in (A), while panels (B)-(D) illustrate the type of behavior that can emerge from a gradual slip response with varying values for the β parameter: (B) $\beta = 0.25$ (stuck), (C) $\beta = 0.30$ (stepping), (D) $\beta = 0.5$ (gliding). (F) Kymograph of the tangential traction stresses as a function of the position along the cell trajectory at a given time for a cell with bond dynamics modeled by Eq. S11 and $\beta = 0.30$. The inclined lines indicate the instantaneous position of the front and rear cell edges while the dashed line represents the cell centroid position. (G) The time evolution of the cell length shows periodic extension-contraction events for a cell with bond dynamics modeled by Eq. S11 and $\beta = 0.30$.
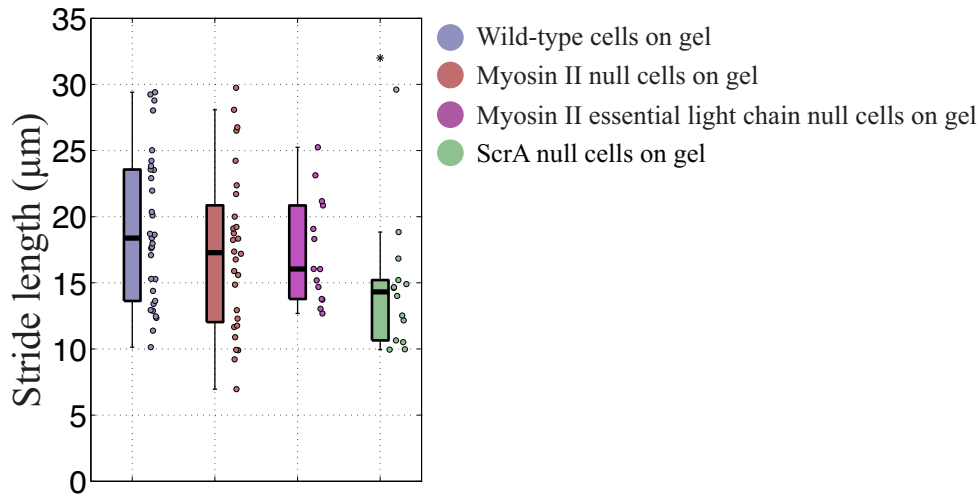
Supplementary Figures:

Figure S5: **Box and whisker plot of the stride length for different cell types.** The boxplots show the quartiles and the median of the distribution of stride length, defined as $\lambda = vf$ where v is the average cell speed and f is the frequency of the motility cycle. The circles represent the value of the stride length for each individual cell in each group. One asterisk denotes statistically significant differences between the medians of two distributions ($p < 0.05$, Wilcoxon ranksum test).

Supplementary Movies:

Supplementary movie 1: **Simulated cell exhibits gliding-like motility when cell-surface interaction is modeled by linearly elastic springs.** Top panel shows the instantaneous cell outline along with the axial traction stresses. The inset is a zoom in view of the ventral part of the cell to show the spatiotemporal dynamics of adhesions. Cell length is plotted as a function of time in the bottom panel.

Supplementary movie 2: **Stepping locomotion is exhibited by a cell with mechanosensitive adhesions to the surface.** Top panel shows the instantaneous cell outline along with the axial traction stresses. The inset is a zoom in view of the ventral part of the cell to show the spatiotemporal dynamics of adhesions. The color and width of the adhesion links is linearly scaled to the bond density; a dark, black link corresponds to full occupancy, i.e., $N = 1$, and lighter, thinner links indicate low density bonds. Cell length is plotted as a function of time in the bottom panel.

Supplementary movie 3: **Transitions in emergent motility modes are reported as a function of the surface binding site density**. For different surface binding site densities, the left-hand side plots show the time evolution of cell length while the right-hand side plots show the instantaneous cell outline along with the axial traction stresses. Four different values of surface binding site density are considered in order of increasing value: $\eta_0 = 0.006, 0.012, 0.016, 0.024$. At low binding site density (top panel), the average cell speed is 20 μm/min and the motion shows small amplitude oscillations in length changes. The identification of the motility mode as gliding is based on the small amplitude of morphological changes (less than 2 μm). As binding site density is increased, we observe a switch in migration mode from gliding to transition (second panel) to stepping (third panel). The identification of the motility mode as gliding is based on the amplitude of morphological changes (average amplitude between 5-8 μm). The mean cell speed decreases while the amplitude of length oscillations
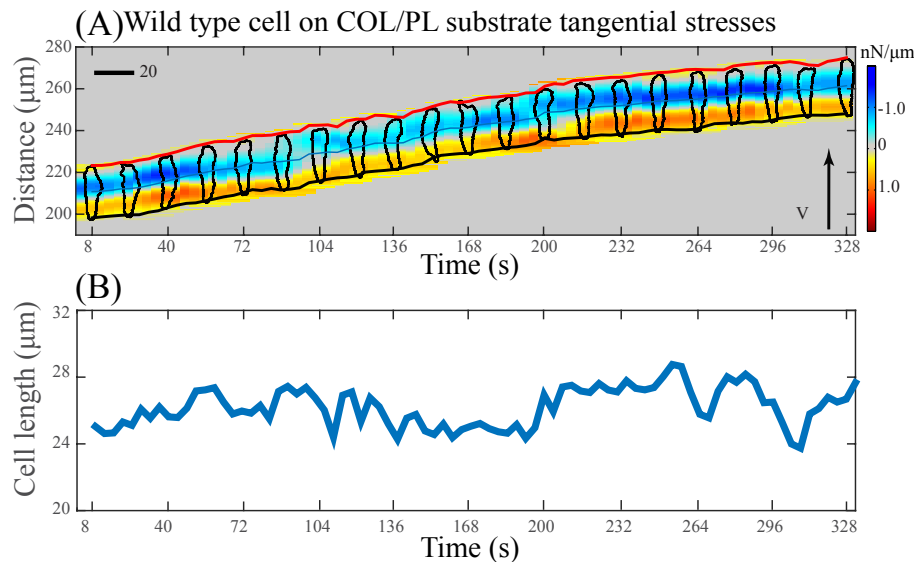
Figure S6: **Gliding-like motility mode in wild-type *Dictyostelium* cells migrating on highly adhesive substrate.** The identification of the motility mode is based on the spatiotemporal patterns of axial traction stresses and small amplitude length changes. (A) Axial traction tension kymograph of a representative chemotaxing wild-type *Dictyostelium* cell on a highly adhesive substrate additionally coated with poly-L-lysine (COL/PL). Cell contour is represented in black. The color map on the right indicates the magnitude of the tangential stresses. The red and black lines indicate the instantaneous front and back edges of the cell respectively while the gray line indicates the instantaneous position of the cell centroid. (B) The corresponding cell length plotted over time shows small amplitude length changes characteristic of a gliding motility mode.

increases. If binding site density is further increased, the cell does not migrate across the surface and its length reaches a plateau value. The motility mode is classified as stationary since the average speed is below 2 μm/min.

Supplementary movie 4: **Simulated cells exhibits recycling of adhesion sites when cell-surface interaction is modeled by non-uniform linearly elastic springs.** The movie shows the instantaneous cell outline along with the axial traction stresses for a cell adhering to the surface only near the cell front and rear. At the end of the motility cycle, what was initially the front adhesion site is now located at the rear of the cell and the cell pulls upward and inward on these adhesion bonds.

Supplemetary References

[1] Alonso-Latorre, B., J. C. del Álamo, E. Bastounis, R. Meili, R. A. Firtel, and J. C. Lasheras, 2010. Spatiotemporal analysis of traction work produced by migrating amoeboid cells. Biophys J. 98:367a-367a.

[2] Bastounis, E., R. Meili, B. Alonso-Latorre, J. Francois, J. C. del Álamo, J. C. Lasheras, and R. A. Firtel, 2011. The SCAR/WAVE complex is necessary for proper regulation of traction stresses during amoeboid motility, Mol. Biol. Cell. 22:3995-4003.

[3] Bastounis, E., R. Meili, B. Álvarez-González, J. Francois, J. C. del Álamo, R. A. Firtel, and J. C. Lasheras, 2014. Both contractile axial and lateral traction force dynamics drive, J. Cell Biol. 204:1045-1061.

[4] del Álamo, J. C., R. Meili, B. Alonso-Latorre, J. Rodríguez-Rodríguez, A. Aliseda, R. A. Firtel, and J. C. Lasheras, 2007. Spatio-temporal analysis of eukaryotic cell motility by improved force cytometry. Proc. Nat. Acad. Sci. USA. 104:13343-13348.
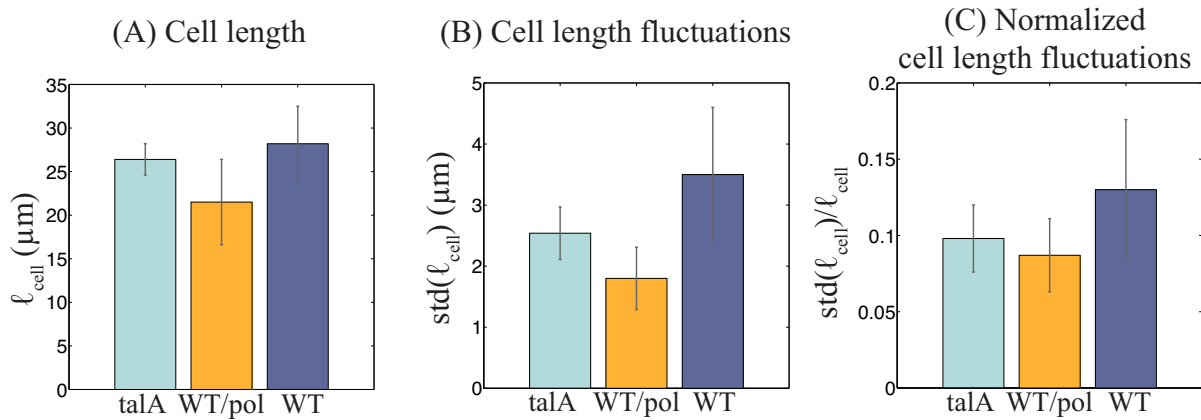
Figure S7: **Talin A-null cells show small length changes similar to those observed in cells on poly-L-lysine coated surfaces.** The cell lines are considered are wild-type (WT) and talin A-null (talA) cells on collagen gel, and wild-type cells on poly-L-lysine coated surfaces (WT/pol) ($N = 6$ for all three cell types). (A) Bar plot of cell length. Wild-type cells on collagen are significantly longer than wild-type cells on poly-L-lysine ($p = 0.012$) but not than talin A-null cells on collagen ($p = 0.36$). (B) Bar plot of standard deviations of cell length temporal fluctuations. Wild-type cells on collagen have significantly larger fluctuations than wild-type cells on poly-L-lysine ($p = 0.002$). There is a trend for wild-type cells on collagen to have larger fluctuations than talin mutants on collagen but it is not statistically significant ($p = 0.076$). (C) Bar plot of standard deviations of cell length normalized with cell length. Wild-type cells on collagen have significantly larger normalized fluctuations than wild-type cells on poly-L-lysine surfaces ($p = 0.041$). There is a trend for wild-type cells on collagen to have larger normalized fluctuations than talin mutants on collagen but it is not statistically significant ($p = 0.16$). Small normalized length fluctuations are observed in both talin A-null mutants and cells on poly-L-lysine, which exhibit a gliding motility mode.

[5] Álvarez-González, B., R. Meili, E. Bastounis, R. A. Firtel, J. C. Lasheras, and J. C. del Álamo, 2015. Three-dimensional balance of cortical tension and axial contractility enables fast amoeboid migration, Biophys. J. 108:1-12.

[6] Alonso-Latorre, B., R. Meili, E. Bastounis, J. C. del Álamo, R. A. Firtel, and J. C. Lasheras, 2009. Distribution of traction forces and intracellular markers associated with shape changes during amoeboid cell migration. 31th Annual International Conference of the IEEE Engineering in Medicine and Biology Society. 3346-3349.

[7] Tse, J. R. and A. J. Engler, 2010. Preparation of hydrogel substrates with tunable mechanical properties. Current protocols in cell biology / editorial board, J. S. Bonifacino et al. Chapter 10:Unit 10-16.

[8] Wang, Y. L. and R. J. Pelham, Jr., 1998. Preparation of a flexible, porous polyacrylamide substrate for mechanical studies of cultured cells. Methods in enzymology. 298:489-496.

[9] Engler, A., L. Bacakova, C. Newman, A. Hategan, M. Griffin, and D. Discher, 2004. Substrate compliance versus ligand density in cell on gel responses. Biophys. J. 86:617-28.

[10] del Álamo, J. C., R. Meili, B. Álvarez-González, B. Alonso-Latorre, E. Bastounis, R. A. Firtel, and J. C. Lasheras, 2013. Three-dimensional quantification of cellular traction forces and mechanosensing of thin substrata by Fourier traction force microscopy. PLoS ONE. 8:e69850.

[11] Dai, J., H. P. Ting-Beall, R. M. Hochmuth, M. P. Sheetz, and M. A. Titus, 1999. Myosin I contributes to the generation of resting cortical tension. Biophys. J. 77:1168-1176.

[12] Gerald, N., J. Dai, H. P. Ting-Beall, and A. De Lozanne, 1998. A role for *Dictyostelium* racE in cortical

tension and cleavage furrow progression. J. Cell Biol. 141:483:492.

[13] Reichl, E. M., Y. Ren, M. K. Morphew, M. Delannoy, J. C. Effler, K. D. Girard, S. Divi, P. A. Iglesias, S. C. Kuo, and D. N. Robinson, 2008. Interactions between myosin and actin crosslinkers control cytokinesis contractility dynamics and mechanics. Curr. Biol. 18:471-480.

[14] Van Haastert, P. J. M, 2010. Chemotaxis: insights from the extending pseudopod. J. Cell Sci. 123:3031-3037.

[15] Novikova E. A., and C. Storm, 2013. Contractile fibers and catch-bond clusters: a biological force sensor? Biophys. J. 105:1336-1345.

[16] Mogilner A., and G. Oster, 1996. Cell motility driven by actin polymerization. Biophys J. 71:3030-3045.

[17] Parekh S. H., O. Chaudhuri, J. A. Theriot, D. A. Fletcher, 2005. Loading history determines the velocity of actin-network growth. Nat. Cell Biol. 7:1219-1223.

[18] Prass M., K. Jacobson, A. Mogilner, M. Radmacher, 2006. Direct measurement of the lamellipodial protrusive force in a migrating cell. J. Cell Biol. 174:767-772.

[19] Heinemann F., H. Doschke, M. Radmacher, 2011. Keratocyte lamellipodial protrusion is characterized by a concave force-velocity relation. Biophys. J. 100:1420-1427.